

Design, Control, and Motion-Planning for a Root-Perching Rotor-Distributed Manipulator

Takuzumi Nishio¹, Moju Zhao², Kei Okada¹, Masayuki Inaba¹

Abstract—Manipulation performance improvement is crucial for aerial robots. For aerial manipulators, the baselink position and attitude errors directly affect the precision at the end effector. To address this stability problem, fixed-body approaches such as perching on the environment using the rotor suction force are useful. Additionally, conventional arm-equipped multirotors, called rotor-concentrated manipulators (RCMs), find it difficult to generate a large wrench at the end effector due to joint torque limitations. Using distributed rotors to each link, the thrust can support each link weight, decreasing the arm joints' torque. Based on this approach, rotor-distributed manipulators (RDMs) can increase feasible wrench and reachability of the end-effector. This paper introduces a minimal configuration of a rotor-distributed manipulator that can perch on surfaces, especially ceilings, using a part of their body. First, we design a minimal rotor-distributed arm considering the flight and end-effector performance. Second, a flight controller is proposed for this minimal RDM along with a perching controller adaptable for various types of aerial robots. Third, we propose a motion planning method based on inverse kinematics (IK), considering specific constraints to the proposed RDMs such as perching force. Finally, we evaluate flight and perching motions and confirm that the proposed manipulator can significantly improve the manipulation performance.

Index Terms—Aerial Manipulator, Aerial Systems, Motion Control, Motion Planning, Perching

I. INTRODUCTION

AERIAL robots, especially multirotor unmanned aerial vehicles (UAVs), have been rapidly improved for various applications in the last few decades. Aerial manipulation is one of the most popular fields, and various types of aerial manipulators have been developed [1]. In [2], one of the earliest aircraft is a helicopter with a heavy and high-performance industrial robotic arm. However, adopting this robot for daily manipulation tasks is difficult owing to its complexity. Therefore, multirotors with various types of arms have been proposed. First, multirotors with a single-link arm were developed (e.g., [3], [4], [5], [6], [7], [8]). During a flight, these aerial robots equipped with rigid arms can achieve an arbitrary 6D pose at the end-effector when the dynamics of the robots are fully actuated [9], [10], [11]. Additionally, the aerial manipulation tasks of under-actuated aerial robots have also increased as the number of joints or arms increased (e.g.,

This paper was recommended for publication by Editor Paolo Robuffo Giordano upon evaluation of the Associate Editor and Reviewers' comments. This work was supported by JSPS KAKENHI Grant ID 22710191.

¹ Department of Mechano-Infomatics, The University of Tokyo, ² Department of Mechanical Engineering, The University of Tokyo, 7-3-1 Hongo, Bunkyo-ku, Tokyo 113-8656, Japan. (corresponding author: Takuzumi Nishio, nishio-takuzumi@ynl.t.u-tokyo.ac.jp).

Digital Object Identifier (DOI): see top of this page.

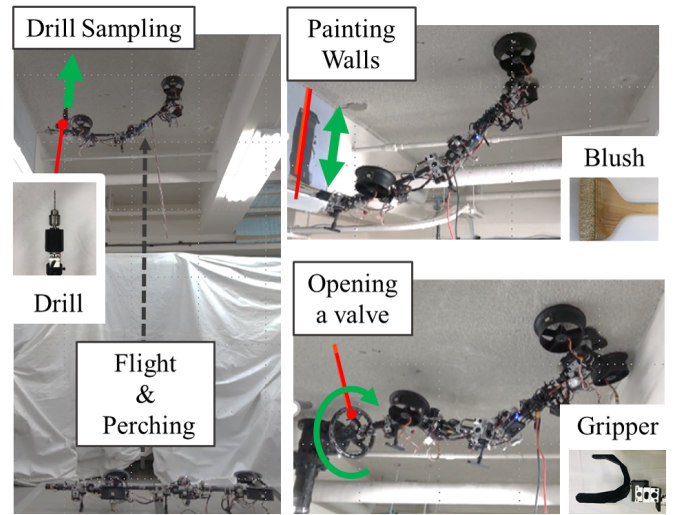


Fig. 1. Aerial manipulator can perch on horizontal surfaces using rotor thrust and perform manipulation tasks, such as drilling, painting, and opening a valve. (URL : <https://www.youtube.com/watch?v=neKcLcekHMY>)

[12], [13]). In [14], [15], and [16], multirotors with the three, six, and seven degrees of freedom (DoF) arm were developed, respectively. Furthermore, multirotors with two and three arms were developed in [17] and [18]. To achieve an arbitrary 6D pose at the end-effector using these under-actuated aerial robots during hovering, dynamics of manipulators are desired to be fully actuated. Therefore, the joint number of robots must be at least six [19]. Using these aerial manipulators, basic manipulation tasks, such as point contact (PC) [14], pick & place (P&P) [20], pull/pushing (PP) [21], sliding (S) [22], and peg-in-hole (PH) [23] can be conducted. In addition, more complex tasks, such as opening a lightweight valve [17] and performing corrosion repairs [24] were conducted.

As mentioned above, the performance of the aerial manipulation has been significantly improved. However, three critical problems need to be solved to improve their performance with regard to more complex tasks: (A) The end effector stability in the air is insufficient for more complex tasks. (B) Owing to the payload capacity, the arm joint-torque limitations are very strict. Therefore, conventional aerial manipulators, i.e., multirotors with arms, can generate a comparatively small wrench at the end-effector. (C) The end-effector motion is disturbed by the concentrated rotors. This causes a reduction in the reachability of the end-effector. To address these problems, we consider the minimal configuration of rotor-distributed manipulators that can perch on the environment.

The perching ability significantly improves the end-effector stability. Thus, the distributed rotors can relax the joint torque limitation and increase the reachability and feasible wrench at the end-effector. Consequently, the proposed manipulator attains complex manipulations such as drilling, painting, and opening a valve, as shown in Fig. 1.

A. Related Work

Conventional aerial manipulators face three challenges: (1) stability, (2) feasible wrench generation, and (3) reachability at the end-effector. In the following sections, we introduce related work and our approaches for address these problems.

1) *Perching Approach to Increase the Stability*: A fixed-body approach, in which robots use an adhesive to perch on surface, is one of the most useful approaches for aerial robots that can be used to improve the precision at the end effector. Previous works have proposed various mechanisms to perch on various surfaces (e.g., [25], [26], [27], [28]). A bio-inspired adhesive that is useful to perch on flat planes has been suggested (e.g., [29], [30]). This approach can significantly reduce their energy consumption as the multirotor is not required to generate thrust during perching. However, this mechanism cannot exert a sufficient force on rough planes. Another popular approach is a gripper (e.g., [31], [32], [33]). This approach is effective for perching on columnar objects such as pipes; however, its mechanics make perching on planes difficult. Magnetic perching is also a popular approach. It can exert comparatively large force only for magnetic metallic objects (e.g., [34], [35]). Additionally, the simplest perching approach for aerial robots is using the rotor suction force. The benefit of this approach is that no additional modules are needed to increase the weight, such as magnets or grippers. In [36], a quadrotor for bridge inspections was developed, and it can perch on ceilings using the rotor thrust. This study also indicated that the perching ability of robots on ceilings is useful for aerial manipulation tasks, such as inspections and repairs. Here, the rotor suction force is varied near ceilings owing to the airflow change, a phenomenon called the ceiling effect. This effect depends on the distance between the rotors and ceilings. Some studies have investigated this ceiling effect (e.g., [37], [38], [39], [40]). Several models have been proposed based on the fluid dynamics (e.g., [41], [42]). In the conventional perching approaches using rotor thrust, the suction force is uncontrolled, and rotors generate excessive thrust. To address this problem, we propose a controller that calculates the minimum rotor thrust to perch.

2) *Rotor-Distributed Manipulator to Increase the End-Effector Feasible Wrench*: To address the small feasible wrench problem at the end effector, the rotor arrangement must be considered. By using distributed rotors on arm links, the rotor thrust can support the arm joint torque. Therefore, the rotor-distributed manipulator (RDM) end-effector can generate a larger wrench than the conventional rotor-concentrated manipulators (RCM). Some aerial robots based on this rotor-distributed approach have been proposed already (e.g., [43], [44], [45], [46]). In [47], a rotor-distributed aerial robot whose links are connected by two servo motors is

developed. Each link has a dual-rotor unit that generates equal thrust. These rotors' thrust relaxes the joint torque limitations. Based on the quadrotor design, each rotor unit is placed at the center of a link. This robot can fly when the numbers of links and rotors are more than four and eight. By utilizing the rotor-distributed approach, the robot can achieve various postures in the air. In [48], a rotor-distributed aerial robot with sixteen rotors, whose links are connected by spherical passive joints and equipped with eight rotors, is proposed. The dynamics of each link is fully actuated, and the rotor arrangement of each link is optimized considering the feasible control wrench as shown in [21]. Using the fix-body approach on the ground, this large-scale robot can complete manipulation task, such as opening a valve. However, the conventional rotor-distributed robots are large and have several rotors, as the end-effector feasible wrench increases as the rotor number and diameter increase. However, it is difficult to use these large robots instead of human arms in narrow spaces. Therefore, a human-scale arm robot that can enter narrow spaces and generate maximum possible wrenches is required. In this study, we propose a minimal configuration of a human-arm-scale RDM, considering the rotor number and arrangement based on flight stability and end-effector performance.

3) *Root-Perching to Increase Reachability*: Based on previous research, we consider the minimal configuration of a human-arm scale RDM that can perch on ceilings using rotor suction force. To increase the reachability at the end-effector, the manipulator only uses a part of its body for perching, such as the root unit. Unlike the conventional RCM, the root unit of the RDM becomes small, and its perching stabilization becomes more difficult. Therefore, it is essential to consider the contact conditions, such as the static friction and zero moment point (ZMP) [49]. Bipedal robots walk using the rotor thrust considering the foot conditions to stabilize their walking in [50] and [51]. In this study, we propose a control method that minimizes the rotor thrust for perching, considering the foot conditions. Furthermore, we propose a motion planner and calculate the reachability of RDMs to evaluate their performance.

In this paper, we introduce the design, control, and motion planning methods for an RDM that can perch on ceilings and evaluate the experimental performance. The key contributions of this paper are as follows:

- 1) We design a minimal RDM with the root perching abilities considering flight stability and end-effector performance. Additionally, we compare its performance compared to the conventional RCM that is composed of identical elements.
- 2) We propose a controller to stabilize perching motions. The perching controller considers contact conditions, such as static friction and ZMP.
- 3) Finally, we propose a motion planning method for the perching RDM considering some constraints such as perching force. This robot attains stable manipulation tasks on actual ceilings.

TABLE I
DEFINITION OF THE MAIN PHYSICAL VARIABLES.

Symbol	Definition
c	Ratio of the rotor thrust to its drag
D_{rotor}	Rotor diameter
\mathbf{F}	Force vector
g	Gravity acceleration
H	Foot size
\mathbf{I}	Moment of inertia
\mathbf{J}	Jacobian matrix
m	Mass
L	Length
\mathbf{M}	Moment vector
\mathbf{p}	Position vector
\mathbf{q}	Joint vector
\mathbf{Q}	Thrust allocation matrix
S	Area
V	Volume
\mathbf{W}	Wrench vector
α	Vectoring apparatus angle in the roll direction
β	Vectoring apparatus angle in the pitch direction
η	XYZ-Euler angle vector
θ	Roll angle
μ	Static friction coefficient
ζ	Pose and joint angles vector
σ	Rotational direction of a rotor
λ	Rotor thrust vector
ξ	Position and attitude vector
ϕ	Pitch angle
τ	Joint torque vector
ψ	Yaw angle
ω	Angular velocity vector

B. Organization

In the following sections, we introduce a human-arm-scale RDM design, control, and motion planning method. We discuss the minimal design of the RDM in Sec. II. In Sec. III, the quasi-static model of the proposed RDM is derived. Based on the model, we propose a flight/perching control and motion planning method in Secs. IV and V. We introduce the system architecture in Sec. VI and evaluate the flight and perching motions in Sec. VII. Finally, the results and future work are discussed in Sec. VIII. The main physical variables in this paper are defined in Table. I.

II. DESIGN

This section introduces the minimal configuration of the human-arm scale RDM. The proposed manipulator is composed of an arm and foot unit to perch on ceilings. Herein, (A) some basic RDMs are introduced, and the number and arrangement of the rotors are determined considering the flight and end-effector performance. In addition, the proposed RDM is compared with the conventional RCM by focusing on the end-effector performance. (B) The detailed configuration of the proposed RDM is explained.

A. Minimal Design of the Rotor-Distributed Manipulator

To clarify the minimal configuration of the RDM, the number of joints N_{joint} , arm links N_{link} , and rotors N_{rotor} need to be determined. The N_{joint} is set to six. For aerial manipulators during flight, no arm joints are required to achieve an arbitrary 6D pose at the end-effector when the robot

dynamics are fully actuated. However, for fixed-base RDMs, six joints are required to achieve arbitrary 6D pose at the end-effector. Here, the maximum DoF of a single joint unit is three such as the ball joint. Therefore, the minimum number of arm links N_{link} for fixed-base RDMs is two such as LASDRA [48]. However, the airflow caused by the end-effector rotor can disturb the manipulation. Furthermore, the reachability space of these two-link RDM is not sufficient considering the rotor unit interference. Therefore, the link number for the proposed RDM is set to three, and the end-effector link is not equipped with any rotors. Furthermore, we choose the link length to attain the human-scale arm as shown in Sec. VI-B. Based on the above discussion, the number and arrangement of rotors is discussed considering the flight and end-effector performance.

1) *Flight Stability by the Number of Rotors*: The flight performance of RDMs mainly depends on the number of rotors N_{rotor} . Several studies have determined the rotor numbers and arrangement for aerial robots with a rigid body ([21] and [52]). However, with these approaches, it is difficult to evaluate the performance of the proposed rotor-distributed robots, as the rotor arrangement varies owing to the joint-angle change. Therefore, we introduce a simple approach to evaluate the flight stability of RDM, called "the aerial zero moment point (aerial ZMP)", which is analogous to the conventional ZMP method [49]. The conventional ZMP approach is used to control the robots on the ground. Robot stability is guaranteed when the ZMP is within the support polygon area determined by foot positions. In steady state, the ZMP corresponds to the projected point of the center of gravity (CoG) \mathbf{p}_{CoG} .

This study evaluated the flight stability of RDM in a steady state. We assumed that the thrust units of RDMs are perpendicular to the ground, and each rotor generates enough thrust and drag moment around its rotational axes. Then, the altitude z and yaw ψ control stability is guaranteed. The position in the horizontal direction x , y is also stabilized using the vectoring apparatus angles or roll/pitch angles ϕ , θ like in conventional multi-rotor robots (e.g., bi-rotor, tri-rotor, quad-rotor). However, it is challenging for the RDM to stabilize the roll/pitch angles only using vectoring apparatus angles owing to the comparatively large modeling errors caused by link-joint angles. In previous studies [48], [45], and [47], all the RDMs used rotor thrust to stabilize the roll/pitch angles. Therefore, it is effective to stabilize the roll/pitch control of RDMs using rotor thrust. Here, this stability is evaluated by the arrangement of rotors and the position of the CoG.

The aerial support polygon (ASP) area S_{ASP} determined by the rotor positions is shown in Fig. 2 (A). This area is determined by

$$S_{ASP} := \{\mathbf{p}_{ASP_{xy}} = \sum_{n=1}^{N_{rotor}} \gamma_i \mathbf{p}_{rotor, i_{xy}} | \gamma_i \geq 0, \sum_{n=1}^{N_{rotor}} \gamma_i = 1\} \quad (1)$$

where the rotor position is $\mathbf{p}_{rotor, i_{xy}} \in \mathbb{R}^{2 \times 1}$. Here, the flight stability is guaranteed when the aerial ZMP $\mathbf{p}_{AZMP_{xy}} \in \mathbb{R}^{2 \times 1}$, and the projected point of the CoG, is within the ASP area in Eq. (1). The detailed derivation is provided in Appendix A.

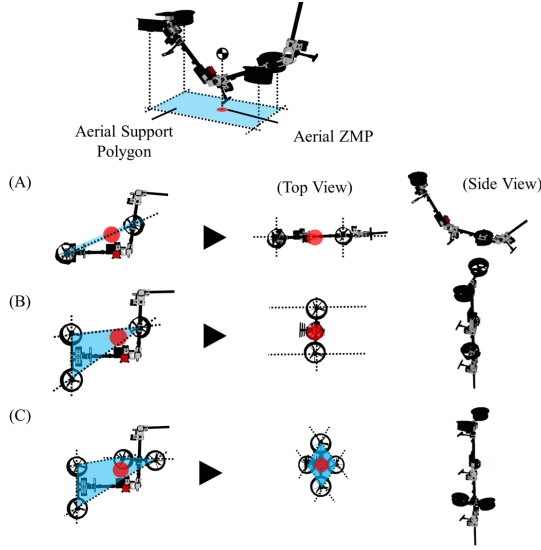


Fig. 2. Aerial zero moment point and support polygon area. (A) Bi-rotor flight stability. (B) Tri-rotor flight stability (C) Quad-rotor flight stability

$$\mathbf{p}_{AZMP_{xy}} \in S_{ASP}, \quad (2)$$

In this study, we consider the basic design of RDMs in steady states, such as bi-rotor, tri-rotor, and quad-rotor RDMs, as shown in Fig. 2 (A)-(C). Each manipulator link is connected by joints. Each rotor unit can be turned upward by joints. We place one rotor unit on the tip of the root link for perching and another at the center of the middle link. No rotors are placed on the end link to prevent from interfering with manipulations. In this study, the distance between rotors on the dual-rotor unit is as small as possible to reduce the joint load caused by the dual-rotor thrust difference, as shown in Figs. 2 (B) and (C).

To evaluate this RDMs stability, we focus on the configuration change. For the bi-rotor RDM, it is difficult to obtain a straight-line configuration during a flight as the S_{ASP} does not exist, as shown in Fig. 2 (A).

Unlike conventional bi-rotors with rigid bodies, actual RDMs cannot easily fly using the change in the rotor unit angles in the air owing to modeling errors of the link-joint angles. For the tri-rotor RDM, only the straight-line configuration flight that is perpendicular to the ground is also difficult, as the S_{ASP} does not exist, as shown in Fig. 2 (B). For the quad-rotor, a straight-line configuration flight that is perpendicular to the ground can be obtained since the aerial ZMP can be within the support polygon area with a margin, as shown in Fig. 2 (C). Therefore, we adopt the quad-rotor as the minimal RDM configuration that can achieve any flight configuration.

2) End-Effector Performance by the Rotor Arrangement:

The arrangement of the rotor units is important for the reachability and feasible wrench at the end-effector. Therefore, a suitable value for evaluating these performances needs to be considered. Several approaches have been proposed to evaluate the manipulator performance. In [53], the manipulability ellipsoid was proposed as an analytical evaluation value for

TABLE II
AMF FOR VARYING ARM VECTORING-APPARATUS POSITION.

Arm Vectoring Apparatus Position	AMF value
Root	0.0
Middle	1.5×10^{-2}
End	3.1×10^{-2}

manipulators. This method can consider actuators' limitations such as joint torque using a weighting matrix [54]. In this study, we introduced a method for evaluating the manipulator performance considering both feasible force and reachability at the end-effector. Here, the reachability space is calculated using inverse kinematics (IK) that considers constraints such as the joint torque. For RDMs, additional constraints such as rotor thrust and stability are considered. The aerial manipulator reachability (AMR) space v_{AMR} and feasible force are calculated using the motion planning approach, as described in Sec.V. Furthermore, the feasible force at the end effector $F_{ee,feasible}$ is considered. $F_{ee,feasible}$ is the maximum force that the end-effector is able to generate at a point in the reachability space.

$$F_{ee,feasible} = \max_j F_{ee,max_j} (j = x, y, z), \quad (3)$$

where $F_{ee,max_j} = \max |F_{ee_j}|$. Based on the above discussion, we defined an aerial manipulator feasibility (AMF) v_{AMF} value that evaluates the reachability and feasible force at the end effector as follows:

$$v_{AMF} = \frac{1}{L^3} \int_{v_{AMR}} \frac{\|F_{ee,feasible}\|}{F} dV, \quad (4)$$

where F , L are the representative force and length of the aerial manipulator. The v_{AMF} is the total value of the end-effector feasible force in the reachability space. It can evaluate both the end-effector reachability and feasible force. Divided by these representative values F , L , this non-dimensionalized AMF value can also be used to compare different lengths and weights manipulators' performance.

A dual-rotor vectoring apparatus with two joints are placed at the tip of the root link for perching on walls. For the

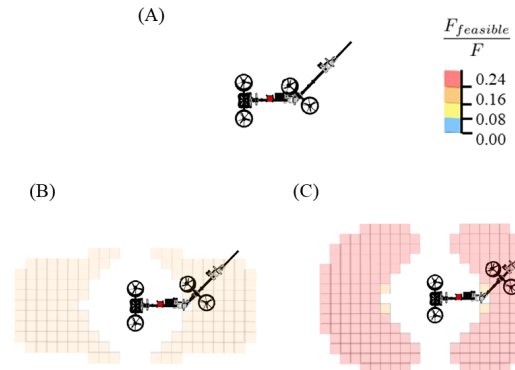


Fig. 3. Reachability due to the arm vectoring apparatus position: (A) root case; (B) middle case; and (C) end case.

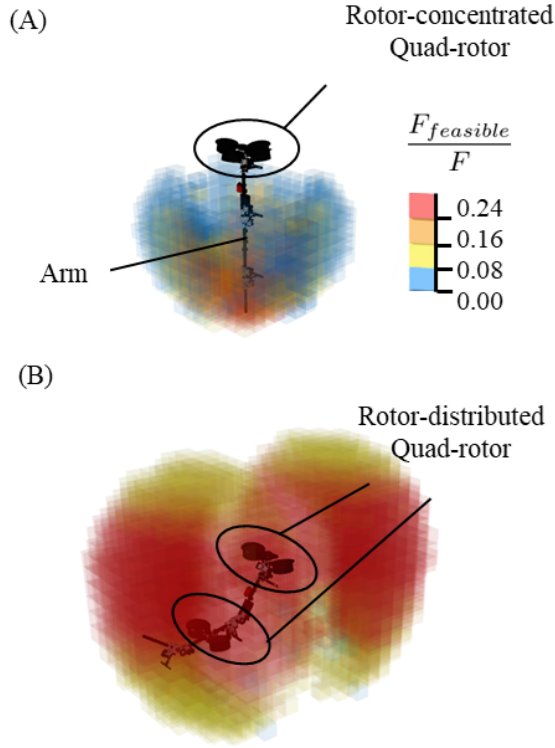


Fig. 4. 3-D reachability space: (A) RCM and (B) RDM

proposed quad-rotor, only the position of the arm vectoring apparatus on the middle link is determined, considering constraints such as rotor thrust limitations. The arm vectoring apparatus position is changed from the root to the end of the middle link to evaluate the end-effector performance as shown in Fig. 3. In the root case, $v_{AMF} = 0.0$ as the arm rotor thrust is insufficient to support the arm weight as shown in Fig. 3 (A). Next, $v_{AMF} = 1.5 \times 10^{-2}$ in the middle case and $v_{AMF} = 3.1 \times 10^{-2}$ in the end case as shown in Table II. These results indicate that the reachability and AMF value are maximums in the end case. Therefore, we place the arm vectoring apparatus at the end of the middle link.

3) *Reachability Comparison*: This study aims to develop a minimal RDM whose performance exceeds conventional RCMs. Therefore, we compared a quadrotor-based RCM and RDM that are composed of identical elements as shown in Fig. 4. As shown in Table III, the AMR of RDM is 2.86 m^2 , which is approximately 2.8 times larger than that of the RCM. Furthermore, the feasible end-effector force of RDM is also larger than that of the RCM as the distributed rotor thrust can

TABLE III
REACHABILITY AND FEASIBILITY OF
QUADROTOR-BASED RCM AND RDM.

Type	AMR [m^2]	AMF value
RCM	1.01	7.5×10^{-2}
RDM	2.86	3.2×10^{-1}
Representative Force		33.5 [N]
Representative Length		1.2 [m]

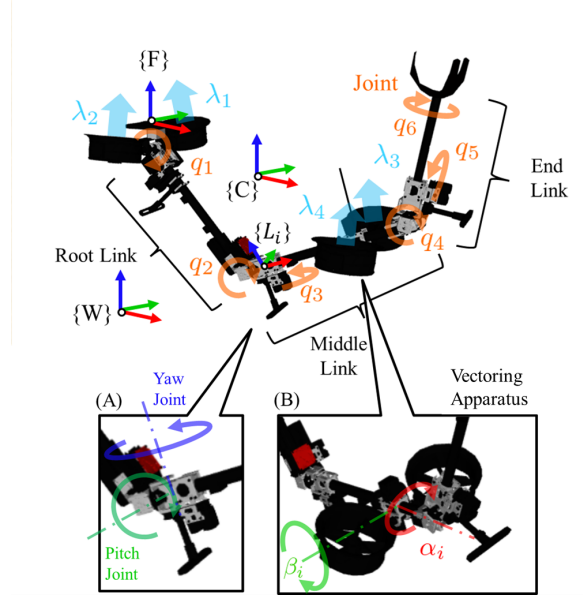


Fig. 5. Robot model of the proposed rotor-distributed manipulator.

relax the joint torque limitations. Therefore, the AMF value of RDM is 3.2×10^{-1} which is approximately forty times larger than that of the RCM.

B. Platform

The main frame link is cylindrical. Each link is connected by two joints q_{2i}, q_{2i+1} ($i = 1, 2$) in the pitch and yaw directions as shown in Fig. 7 (A). These joints are changed from -90 to 90 deg. Here, the sum of the joint numbers is six, as the root pitch q_1 and end-effector roll q_6 joints are equipped. The vectoring apparatus of the arm link has two joints in the roll and pitch directions α_i, β_i to turn the thrust direction upward as shown in Fig. 5 (B). These joints can be changed from -180 to 180 deg. Here, the distance between the two rotors on a vectoring apparatus is as small as possible to reduce the load of the vectoring apparatus around the roll joint. We denote each rotor thrust λ_i ($i = 1, 2, 3, 4$). The foot vectoring apparatus is placed at the tip of the root link to perch on ceilings. The footplate is approximated to the rectangle that has a wrench sensor to estimate the contact conditions. In addition, the end-effector unit can be replaced by a drill, brush, or gripper. The processor and control board are placed at the tip of the root link to increase the end-effector feasible force. The software system is explained in Sec. VI-B.

In this section, we introduced the quadrotor-based RDM with three links and six joints, considering the aerial ZMP for flight stability evaluation. To improve the manipulation performance, we determine the rotor arrangement considering the reachability and feasible force at the end-effector. Furthermore, we demonstrate that the proposed RDM performance significantly exceeds the conventional RCM composed of identical components. Finally, we explain the detailed configuration of the proposed manipulator.

III. MODEL

In this section, we derive a model for flight and perching control of RDMs. The following coordinate systems and notation conventions are used to describe the model. We use four coordinate frames as shown in Fig. 5: the world frame \mathcal{W} , foot frame \mathcal{F} , CoG frame \mathcal{C} , and i -th link frame \mathcal{L}_g . The world frame is fixed on the ground with its z -axis pointing upwards. The foot frame is located on the footplate, its origin is at the center of the footplate, and its y -axis corresponds to the rotational axis of the root joint. In addition, the CoG frame is located at the center of mass, and its x and y axes are aligned with those in the foot frame. Finally, each link frame origin is on the tip of the i -th main link. Their x -axes correspond to the respective axial direction of the i -th main frame. Furthermore, we use the following notation conventions: the vector ${}_{\mathcal{W}}\mathbf{r}$ represents the vector \mathbf{r} in coordinate system \mathcal{W} . In addition, the matrix ${}_{\mathcal{X}}^{\mathcal{Y}}R$ denotes the rotational matrix that rotates a vector in the coordinate system \mathcal{X} to \mathcal{Y} .

A. Quasi-Steady Model for the Rotor-Distributed Manipulator

For the modelling, we use the Newton-Euler formalism. The model of an articulated robot with distributed rotors is described as follows:

$$\begin{bmatrix} \mathbf{H}_{11} & \mathbf{H}_{12} \\ \mathbf{H}_{21} & \mathbf{H}_{22} \end{bmatrix} \begin{bmatrix} \ddot{\boldsymbol{\xi}} \\ \ddot{\mathbf{q}} \end{bmatrix} + \begin{bmatrix} \mathbf{l}_{pose} \\ \mathbf{l}_{joint} \end{bmatrix} = \begin{bmatrix} \mathbf{O}_{6 \times 1} \\ \boldsymbol{\tau}_{joint} \end{bmatrix} + \mathbf{J}_{rotor}^T \begin{bmatrix} \mathbf{F}_{rotor} \\ \mathbf{M}_{rotor} \end{bmatrix} + \sum_{i=1}^{N_{contact}} \mathbf{J}_{contact,i}^T \begin{bmatrix} \mathbf{F}_{contact_i} \\ \mathbf{M}_{contact_i} \end{bmatrix} + \sum_{i=1}^{N_{part}} \mathbf{J}_{part_i}^T(\mathbf{q}) m_{part,i} \mathbf{g}, \quad (5)$$

where $\ddot{\boldsymbol{\xi}} = [\ddot{\mathbf{p}}^T, \dot{\boldsymbol{\omega}}^T]^T$. Here, $\mathbf{p} \in \mathbb{R}^{3 \times 1}$ and $\boldsymbol{\omega} \in \mathbb{R}^{3 \times 1}$ represent the position and angular velocity of the CoG, respectively. $\mathbf{q} \in \mathbb{R}^{N_{joints} \times 1}$ is the vector of the joint and vectoring apparatus angles. The second term on the left side of the equation represents the effects of the Coriolis and centrifugal forces. On the right side, $\boldsymbol{\tau}_{joint} \in \mathbb{R}^{N_{joints} \times 1}$ is the joint torque. $\mathbf{F}_{rotor} \in \mathbb{R}^{3 \times 1}$ and $\mathbf{M}_{rotor} \in \mathbb{R}^{3 \times 1}$ in the second term represent the force and moment, respectively, caused by the rotors' thrust. In addition, $\mathbf{F}_{contact_i} \in \mathbb{R}^{3 \times 1}$ and $\mathbf{M}_{contact_i} \in \mathbb{R}^{3 \times 1}$ are the contact force and moment at the i -th contact part. The final term is the effect caused by gravity. Here, $m_{part,i}$ is the mass of the i -th part, and \mathbf{g} is the gravity acceleration vector. Furthermore, $N_{contact}$ and N_{part} are the number of contact points and robot parts. \mathbf{J} is the Jacobian matrix of each component. From Eq. (5), we derive a robot model for the RDMs. Assuming that the maneuvering with the joint motion of the manipulator is in a quasi-steady state ($\ddot{\mathbf{q}} \approx \mathbf{0}$ and $\dot{\mathbf{q}} \approx \mathbf{0}$), the manipulator translational motion at the \mathcal{W} coordinate and rotational motion at the \mathcal{C} coordinate are given by

$$\begin{bmatrix} m\mathbf{E} & \mathbf{O}^{3 \times 3} \\ \mathbf{O}^{3 \times 3} & \mathbf{I}(\mathbf{q}) \end{bmatrix} \begin{bmatrix} \ddot{\mathbf{p}} \\ \dot{\boldsymbol{\omega}} \end{bmatrix} + \begin{bmatrix} \mathbf{O}^{3 \times 1} \\ \boldsymbol{\omega} \times \mathbf{I}(\mathbf{q}) \boldsymbol{\omega} \end{bmatrix} = \begin{bmatrix} \mathbf{F}_{rotor}(\boldsymbol{\lambda}_{rotor}, \mathbf{q}) \\ \mathbf{M}_{rotor}(\boldsymbol{\lambda}_{rotor}, \mathbf{q}) \end{bmatrix} + \begin{bmatrix} \mathbf{F}_{foot} \\ \mathbf{M}_{foot} \end{bmatrix} + \begin{bmatrix} \mathbf{F}_{ee} \\ \mathbf{M}_{ee} \end{bmatrix} + \begin{bmatrix} m\mathbf{g} \\ \mathbf{O}^{3 \times 1} \end{bmatrix}, \quad (6)$$

where m and $\mathbf{I}(\mathbf{q})$ are the robot mass and moment of inertia, respectively. \mathbf{F}_{rotor} and \mathbf{M}_{rotor} are the force and moment caused by rotor thrust $\boldsymbol{\lambda}_{rotor} \in \mathbb{R}^{N_{rotor} \times 1}$ and joint angles, respectively. \mathbf{F}_{foot} , \mathbf{M}_{foot} and \mathbf{F}_{ee} , \mathbf{M}_{ee} are the force and moment on the footplate and at the end-effector, respectively, and $\mathbf{g} = [0, 0, -g]^T$ using gravity acceleration g . In Eq. (6), the relationship between the wrench caused by rotor $\mathbf{W}_{rotor} = [\mathbf{F}_{rotor}^T, \mathbf{M}_{rotor}^T]^T$ and $\boldsymbol{\lambda}_{rotor}$ is nonlinear. Therefore, the cost incurred to calculate the desired rotor thrust is high. To reduce this cost, we assume that the vectoring apparatus is horizontal in the world coordinate. Consequently, $\mathbf{W}_{rotor}(\mathbf{q})$ in the \mathcal{C} coordinate is expressed by

$$\mathbf{W}_{rotor}(\mathbf{q}) = \mathbf{Q}(\mathbf{q}) \boldsymbol{\lambda}_{rotor}, \quad (7)$$

where the rotor allocation matrix $\mathbf{Q}(\mathbf{q})$ is given by:

$$\begin{aligned} \mathbf{Q}(\mathbf{q}) &= \begin{bmatrix} \mathbf{u}_1(\mathbf{q}) & \cdots & \mathbf{u}_i(\mathbf{q}) & \cdots & \mathbf{u}_{N_{rotor}}(\mathbf{q}) \\ \mathbf{v}_1(\mathbf{q}) & \cdots & \mathbf{v}_i(\mathbf{q}) & \cdots & \mathbf{v}_{N_{rotor}}(\mathbf{q}) \end{bmatrix}, \quad (8) \\ \mathbf{v}_i(\mathbf{q}) &= ([\mathbf{p}_{rotor_i}(\mathbf{q}) \times] - c\sigma_i) \mathbf{u}_i(\mathbf{q}), \quad (9) \end{aligned}$$

where $\mathbf{u}_i(\mathbf{q})$ is the unit normal on the rotational plane, and $\sigma_i (= (-1)^{i+1})$ is the rotational direction of the i -th rotor. Thus, c is the ratio of the rotor thrust to its drag around the rotational axis. Based on the above model, we calculate the desired rotor thrust during a flight as described in Sec. IV-A.

B. Contact Stability Constraints

For stable perching, the additional constraints at each contact point should be considered. To prevent slipping on walls, we consider the Coulomb friction constraints. Then, a contact force $\mathbf{F}_{contact_i}$ satisfies the following relationships:

$$\mathbf{F}_{contact_i} \cdot \mathbf{n}_{contact_i} > 0, \quad (10)$$

$$\begin{aligned} \|\mathbf{F}_{contact_i} - (\mathbf{F}_{contact_i} \cdot \mathbf{n}_{contact_i}) \mathbf{n}_{contact_i}\| \\ \leq \mu_j (\mathbf{F}_{contact_i} \cdot \mathbf{n}_{contact_i}), \quad (11) \end{aligned}$$

where $\mathbf{n}_{contact_i}$ is a unit normal to the contact surface, and μ_j ($j = x, y$) is the static friction coefficient. Approximating the contact wrench cone (CWC) in Eq. (11) to a pyramid, the foot force \mathbf{F}_{foot} satisfies the following conditions:

$$F_{foot_z} > 0, \quad (12)$$

$$|F_{foot_j}| \leq \mu_j F_{foot_z} \quad (j = x, y). \quad (13)$$

In addition, we should prevent rotation during perching. Considering the rotational static friction, the constraint is given by

$$\begin{aligned} \|\mathbf{M}_{contact_i,z}\| \\ < M_{contact_i,z}(\mathbf{F}_{contact_i}, \mathbf{M}_{contact_i}), \quad (14) \end{aligned}$$

where $M_{contact_i,z}(\mathbf{F}_{contact_i}, \mathbf{M}_{contact_i})$ is the maximum rotational static friction moment. Assuming $M_{contact_i,z}(\mathbf{F}_{contact_i}, \mathbf{M}_{contact_i}) = \mu_z F_{contact_i,z}$ in Eq. (14), the condition is written as follows:

$$|M_{foot_z}| \leq \mu_z F_{foot_z}, \quad (15)$$

where M_{foot} is the foot moment, and μ_z is the rotational static friction coefficient. For the surface contact, the ZMP $p_{ZMP_i_j}$ ($j = x, y$) at the i -th contact surface should be within the support polygon area S_i to prevent the i -th foot plate from peeling from the surface. Then, the constraint is given by

$$p_{ZMP_{i_x}}, p_{ZMP_{i_y}} \in S_i. \quad (16)$$

Here, the relationship between the ZMP and the contact wrench is given by

$$p_{ZMP_i} \times F_{contact_i} + M_{contact_i} = \mathbf{0}, \quad (17)$$

where $p_{ZMP_i} = [p_{ZMP_i, x}, p_{ZMP_i, y}, p_{ZMP_i, z}]$. Using the boundary points p_{bound_j} ($j = 1, \dots, N_{bound}$) in the foot plate area S_{foot} , the ZMP constraints in Eq. (16) are expressed by

$$p_{ZMP_i, x}, p_{ZMP_i, y} \in \left\{ \sum_{j=1}^{N_{bound}} \gamma_j p_{bound_j} \mid p_{bound_j} \in S_{foot} \right\}, \quad (18)$$

where N_{bound} is the number of boundary points. γ_i satisfies the following constraints:

$$\begin{cases} \gamma_j \geq 0 \\ \sum_{j=1}^{N_{bound}} \gamma_j = 1. \end{cases} \quad (19)$$

Considering these constraints for calculating the rotor thrust, we achieve stable perching control as described in Sec. IV-B.

In this section, we introduce a model of rotor-distributed robots in a quasi-steady state and under contact stability constraints, such as static friction and ZMP. Using these models, we propose a control method of the proposed minimal RDM for flight and perching.

IV. CONTROL

Our goal is to determine the rotor thrust and vectoring apparatus angles. Here, the desired rotor thrust is expressed as follows:

$$\lambda_{rotor} = \lambda_{flight} + \lambda_{perch}, \quad (20)$$

where λ_{flight} is the thrust for flight, and λ_{perch} is the additional thrust for perching. To decrease the computational cost, we use a linearized model and propose a controller for under-actuated robots based on the back-stepping control framework. This method for minimal RDMs would be adopted to the RDMs with an increased number of links and rotors. The variable with the notation tilde represents the estimated value.

A. Flight Control

To achieve stable maneuvering with joint motion during flight, we propose a new control method that determines rotor thrust, attitude, and vectoring apparatus angles based on the conventional under-actuated control method. In the following sections, we introduce (1) attitude and altitude control and (2) position control in a horizontal plane.

1) *Attitude and Altitude Control*: To stabilize the attitude and altitude, the rotor thrust λ_{flight} is calculated using the linear quadratic integral (LQI) control method [45]. From Eq.(6), the linearized equation for altitude and attitude is given by

$$\begin{aligned} \dot{x} &= Ax + B(q)\lambda_{flight} + D, \\ y &= Cx. \end{aligned} \quad (21)$$

Here, each matrix in Eq. (21) is expressed by

$$\begin{aligned} x &= \begin{bmatrix} \bar{\xi} \\ \xi \end{bmatrix}, \quad A = \begin{bmatrix} \mathbf{O}^{4 \times 4} & \mathbf{E}^{4 \times 4} \\ \mathbf{O}^{4 \times 4} & \mathbf{O}^{4 \times 4} \end{bmatrix}, \quad B = \begin{bmatrix} \mathbf{O}^{4 \times N_{rotor}} \\ \bar{M}^{-1} \bar{Q}(q) \end{bmatrix}, \\ C &= \begin{bmatrix} \mathbf{E}^{4 \times 4} \\ \mathbf{O}^{4 \times 4} \end{bmatrix}, \quad D = \begin{bmatrix} \mathbf{O}^{4 \times 1} \\ -g \\ -\mathbf{I}^{-1}(q)(\omega \times \mathbf{I}(q) \omega) \end{bmatrix}, \quad (22) \\ \bar{M} &= \begin{bmatrix} m & \mathbf{O}^{1 \times 3} \\ \mathbf{O}^{3 \times 1} & \mathbf{I}(q) \end{bmatrix}, \end{aligned}$$

where $\bar{\xi}$ and $\bar{Q}(q)$ are the third to sixth rows of ξ and $Q(q)$.

Note that $W_{foot} = \mathbf{O}^{6 \times 1}$ in Eq.(21) during a flight. For the LQI control, we define the following values.

$$\bar{\xi} = \xi - \xi_s, \quad (23)$$

$$\bar{\lambda}_{flight} = \lambda_{flight} - \lambda_{flight,s}, \quad (24)$$

where ξ_s and $\lambda_{flight,s}$ are steady values. When we define the tracking error $e = x - x_s$, the integral value v is given by

$$\dot{v} = y_s - y = -Ce. \quad (25)$$

From Eqs.(21), (23), and (25), the modified equation is expressed as follows:

$$\dot{\bar{x}} = \bar{A} \bar{x} + \bar{B}(q) \bar{\lambda}_{flight}, \quad (26)$$

$$\bar{x} = \begin{bmatrix} e \\ v \end{bmatrix}, \quad \bar{A} = \begin{bmatrix} A & \mathbf{O}_{8 \times 4} \\ -C & \mathbf{O}_{4 \times 4} \end{bmatrix}, \quad \bar{B}(q) = \begin{bmatrix} B(q) \\ \mathbf{O}_{4 \times N_{rotor}} \end{bmatrix}.$$

The cost function is defined as follows:

$$J = \int_0^{\infty} (\bar{x}^T W_1 \bar{x} + \bar{\lambda}_{flight}^T W_2 \bar{\lambda}_{flight}) dt, \quad (27)$$

where W_1 and W_2 are weight matrices. By solving the algebraic Riccati equation (ARE), the optimal control input is obtained by

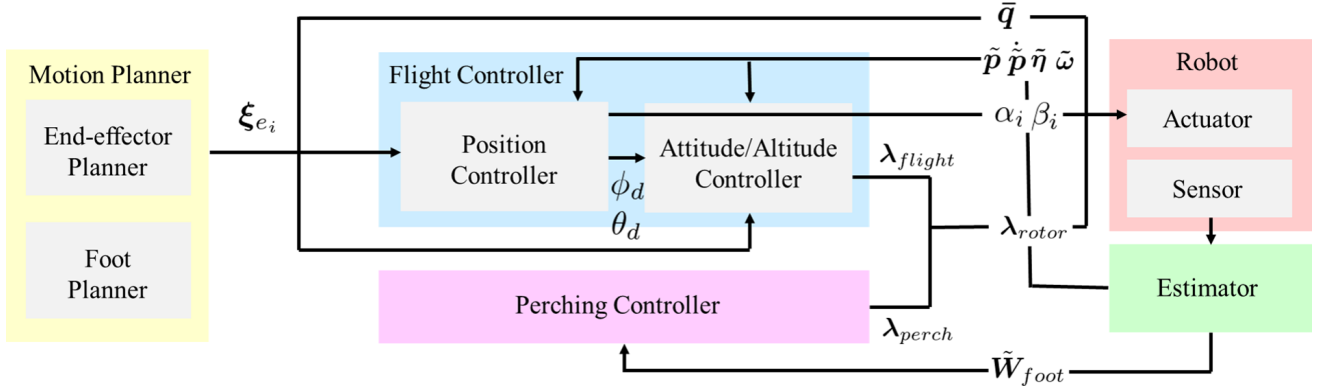


Fig. 6. Control flow for the proposed perching manipulator

$$\lambda_{flight} = \mathbf{K}_x \bar{\mathbf{x}} + \lambda_{flight,s}, \quad (28)$$

where $\lambda_{flight,s}$ is used to support the gravity and gyro moment effect. However, we can ignore the effect of gravity, as the integral feedback term guarantees this effect. Therefore, the thrust for the flight is given by

$$\lambda_{flight} = \mathbf{K}_x \bar{\mathbf{x}} + \bar{\mathbf{Q}}(\mathbf{q})^{-1} \begin{bmatrix} 0 \\ \boldsymbol{\omega} \times \mathbf{I}(\mathbf{q}) \boldsymbol{\omega} \end{bmatrix}. \quad (29)$$

Using the thrust in Eq. (29), we control the attitude and altitude. Next, the position control method is introduced in a horizontal plane.

2) *Position Control in the Horizontal Plane:* In previous studies, only the attitude in the roll and pitch directions were used for position control of under-actuated robots in the horizontal plane [45]. However, this method is difficult to adopt for three-dimensional maneuvering with the joint motion of RDMs owing to the poor responsiveness caused by the significant moment of inertia. Therefore, both attitude and vectoring apparatus angles are used to control the x - and y -directions. Here, we assume that these angles are sufficiently small and do not affect the attitude and altitude control. Using the PID control, the desired acceleration $\ddot{p}_{j,d}$ ($j = x, y$) is given by

$$\ddot{p}_{j,d} = k_{P_j} e_j + k_{I_j} \int e_j dt + k_{D_j} \frac{d}{dt} e_j \quad (j = x, y), \quad (30)$$

where e_j is the state error in the world coordinate. Further, k_{P_j} , k_{I_j} , and k_{D_j} are the PID gains. Using the conventional approach, the aerial robot can be stabilized using the attitude in the roll and pitch angles as follows:

$$\phi_d = k_{\phi_d} \frac{\ddot{p}_{x,d} \sin \psi_d - \ddot{p}_{y,d} \cos \psi_d}{g}, \quad (31)$$

$$\theta_d = k_{\theta_d} \frac{\ddot{p}_{x,d} \cos \psi_d + \ddot{p}_{y,d} \sin \psi_d}{g}. \quad (32)$$

During the flight of the proposed manipulator, it is desirable for the posture to approximate a straight, as the stability and thrust margin become significant considering the aerial ZMP.

In the above situations, it is challenging to stabilize the flight in the x direction owing to the response latency of the pitch angle, as the moment of inertia in the pitch direction increases significantly. To address this problem, we set $\phi_d = 0$ and use the i -th vectoring apparatus angles α_i and β_i as follows:

$$\alpha_i = \tan^{-1} \left(\frac{-n_{\alpha_{iy}}}{n_{\alpha_{iz}}} \right), \quad (33)$$

$$\beta_i = \tan^{-1} \left(\frac{n_{\beta_{ix}}}{-n_{\beta_{iy}} \sin \alpha_i + n_{\beta_{iz}} \cos \alpha_i} \right), \quad (34)$$

where the n_{α_i} and n_{β_i} are expressed by

$$\mathbf{n}_{j_i} = \frac{\mathbf{n}_{va,j_i}}{\|\mathbf{n}_{va,j_i}\|} \quad (j = \alpha, \beta), \quad (35)$$

$$\mathbf{n}_{va,j_i} = {}_{L_i} \mathbf{R} \begin{bmatrix} k_{\theta_i} (\ddot{p}_{x,d} \cos \psi_d + \ddot{p}_{y,d} \sin \psi_d) \\ k_{\phi_i} (\ddot{p}_{x,d} \sin \psi_d - \ddot{p}_{y,d} \cos \psi_d) \\ g \end{bmatrix}, \quad (36)$$

where α_i cannot be used for position control owing to the joint torque limitation as the rapid changes of the vectoring apparatus also generates the large torque on the roll joint in addition to the dual rotor thrust difference. Based on the above discussion, we determine the above gains k in experiments as shown in Sec. VII. Using the controller mentioned above, we stabilize the proposed RDM with a minimal configuration.

B. Perching

A method for perching on surfaces is proposed to calculate the additional thrust for perching $\lambda_{perch,t}$ at the time t . To minimize the thrust, we use the following framework.

$$\min_{\lambda_{perch,t}} \lambda_{perch,t}^T \mathbf{N} \lambda_{perch,t}, \quad (37)$$

where $\lambda_{perch,t}$ should be determined considering the foot contact conditions. To achieve stable perching, we define the perching thrust as follows:

$$\begin{aligned} \lambda_{perch,t} &= \lambda'_{perch,t} + \lambda''_{perch,t}, \\ \mathbf{U}_{mask}(\bar{\mathbf{Q}}_{perch}(\mathbf{q}) \lambda'_{perch,t} - \mathbf{W}_{foot,t}) &= \mathbf{O}, \\ \mathbf{U}_{mask}(\bar{\mathbf{Q}}_{perch}(\mathbf{q}) \lambda''_{perch,t} - \mathbf{W}_{foot,t-1} - \tilde{\mathbf{W}}_{foot}) &= \mathbf{O}, \end{aligned} \quad (38)$$

where \bar{Q}_{perch} is the thrust allocation matrix for perching, and U_{mask} is the matrix used to select the control wrench. Furthermore, $\lambda'_{perch,t}$ is determined by considering the constraints of the foot conditions. $\lambda''_{perch,t}$ is the feedback term that compensates the foot wrench errors. To increase end-effector stability, we use the force perpendicular to the contact plane that is generated by the foot rotors. Based on this strategy, we determine $W_{foot,t}$ considering constraints such as static friction, moment, and ZMP. From Eqs. (13) and (15), the slipping prevention constraints in the foot coordinate are expressed by

$$F_{foot_z,t} > \epsilon_z, \quad (39)$$

$$|\tilde{F}_{foot_j}| < \mu_x F_{foot_z,t} \quad (j = x, y), \quad (40)$$

$$|\tilde{M}_{foot_z}| < \mu_z F_{foot_z,t}, \quad (41)$$

where $\epsilon_z (> 0)$ is a sufficiently small offset value. To prevent peeling from surfaces, the ZMP should be within the footplate area. Assuming the support polygon area is rectangular, the ZMP constraints in Eq. (18) can be represented by

$$-H_j \leq p_{ZMP_j} \leq H_j \quad (j = x, y), \quad (42)$$

where H_j is the half-length of each rectangle edge. The ZMP can be expressed by

$$p_{ZMP_x} = \frac{\tilde{F}_{foot_x} \times p_{ZMP_z} - \tilde{M}_{foot_y}}{F_{foot_z,t}} \quad (43)$$

$$p_{ZMP_y} = \frac{\tilde{F}_{foot_y} \times p_{ZMP_z} + \tilde{M}_{foot_x}}{F_{foot_z,t}}. \quad (44)$$

Additionally, the rotor thrust limitations must be considered and are as follows:

$$\lambda_{min} \leq \lambda_{perch,t} \leq \lambda_{max}, \quad (45)$$

where λ_{min} and λ_{max} are the minimum and maximum limitations of the rotor thrust, respectively. These values are given by

$$\lambda_{min} = \mathbf{O}^{N_{rotor} \times 1}, \quad (46)$$

$$\lambda_{max} = \lambda_{rotor_{max}} + \bar{Q}^{-1}(q)m\tilde{g}, \quad (47)$$

where $\lambda_{rotor_{max}}$ is the maximum thrust for each rotor, and $\tilde{g} = [-g, 0, 0, 0]^T$. Furthermore, the thrust must be changed continuously. Therefore, the following constraint is defined.

$$|\lambda_{perch,t} - \lambda_{perch,t-1}| \leq \delta\lambda_{perch}, \quad (48)$$

where $\delta\lambda_{perch}$ is the limitation of the rotor thrust change at each step. From the above discussion, the perching thrust is calculated by the following quadratic programming (QP) problem.

$$\begin{aligned} \min_{\lambda_{perch,t}} \quad & \lambda_{perch,t}^T N \lambda_{perch,t}, \\ \text{s.t.} \quad & \end{aligned} \quad (49)$$

Eqs. (38), (39), (40), (41), (42), (45), and (48).

Using the proposed perching control, we stabilize the motion of the RDM motion on ceilings.

In this section, we propose a flight and perching controller to stabilize the RDMs. The flight position controller uses both attitude and vectoring apparatus angles. The QP-based flight controller considers foot conditions such as static friction and ZMP.

V. PLANNING

This section proposes a motion generation method for perching RDMs in the steady state. For applications, it is critical for the proposed RDM to achieve the desired end-effector pose. To generate the desired end-effector trajectories, the following framework is used based on differential kinematics:

$$\min_{\delta\zeta_k} G(\delta\zeta_k), \quad (50)$$

$$\zeta_{k+1} = \zeta_k + \delta\zeta_k. \quad (51)$$

First, $\delta\zeta_k$ is determined to minimize the cost function $G(\cdot)$ as shown in Eq.(50). ζ_k is updated using $\delta\zeta_k$ as shown in Eq. (51). Here, the state variables are $\zeta_k = [p_k^T, \eta_k^T, q_k^T]^T$ and $\eta_k = [\phi_k, \theta_k, \psi_k]^T$ at the step k . Then, the pose of the i -th robot end-effector ξ_{e_i} can be expressed by

$$\xi_{e_i} = f_{e_i}(\zeta), \quad (52)$$

When $J_{e_i} = \partial f / \partial \zeta$, the relationship between $\delta\xi_{e_i}$ and $\delta\zeta$ is expressed by

$$\delta\xi_{e_i} = J_{e_i} \delta\zeta, \quad (53)$$

where $J_{e_i} \in \mathbb{R}^{6 \times 6 + N_{joint} + N_{va}}$, and N_{va} is the number of vectoring apparatus joints. Here, we determine $\delta\xi_{e_i}$ as follows:

$$\delta\xi_{e_i} = \kappa \frac{\xi_{e_{i_d}} - \xi_{e_{i_k}}}{\|\xi_{e_{i_d}} - \xi_{e_{i_k}}\|}, \quad (54)$$

where $\xi_{e_{i_d}}$ and $\xi_{e_{i_k}}$ are the final target pose and k -th pose of the i -th end-effector, and $\kappa (> 0)$ is sufficiently small value. Next, we consider the cost function $G(\zeta_k)$. To minimize the updated values, the first cost term is expressed as the following quadratic form:

$$\delta\zeta_k^T S_1 \delta\zeta_k. \quad (55)$$

According to the relationship in Eq. (53), the constraint on the Cartesian motion in the operating space ξ_{e_i} should be equality. However, it is difficult to calculate smooth trajectories using this constraint. Therefore, we consider the following quadratic residual term:

$$\sum_{i=0}^{N_{ee}} (J_{e_i} \delta\zeta_k - \delta\xi_{e_i})^T S_2 (J_{e_i} \delta\zeta_k - \delta\xi_{e_i}), \quad (56)$$

where N_{ee} is the number of end-effectors. S_1 and S_2 are the positive definite diagonal weight matrices. For the proposed

aerial manipulator, we have to consider the end-effector pose ξ_{ee} and foot pose ξ_{foot} as the operating space ξ_{e_i} . Therefore, the cost function is given by

$$G(\zeta_k) = \delta\zeta_k^T S_1 \delta\zeta_k + (\mathbf{J}_{ee} \delta\zeta_k - \delta\xi_{ee})^T S_2' (\mathbf{J}_{ee} \delta\zeta_k - \delta\xi_{ee}) + (\mathbf{J}_{foot} \delta\zeta_k - \delta\xi_{foot})^T S_2'' (\mathbf{J}_{foot} \delta\zeta_k - \delta\xi_{foot}), \quad (57)$$

where $S_2 = \text{diag}[S_2', S_2'']^T$. Furthermore, \mathbf{J}_{ee} and \mathbf{J}_{foot} are the Jacobians of the end-effector and foot pose. To generate the trajectory based on the above framework, we consider the following constraints to minimize the cost function in Eq.(50).

1) *Robot State*: The bound for the robot state owing to the configuration is important to generate the trajectory. Here, the velocity damper [55] is applied to avoid limitations such as joint angles.

$$\delta\zeta^- \leq \delta\zeta_k \leq \delta\zeta^+, \quad (58)$$

$$\delta\zeta^- = \begin{cases} \delta\zeta_{min} \frac{(\zeta_k - \zeta_{min}) - \zeta_F}{\zeta_R - \zeta_F} & (\zeta_k - \zeta_{min} < \zeta_R) \\ \delta\zeta_{min} & (\text{otherwise}) \end{cases}, \quad (59)$$

$$\delta\zeta^+ = \begin{cases} \delta\zeta_{max} \frac{(\zeta_{max} - \zeta_k) - \zeta_F}{\zeta_R - \zeta_F} & (\zeta_{max} - \zeta_k < \zeta_R) \\ \delta\zeta_{max} & (\text{otherwise}) \end{cases} \quad (60)$$

where ζ_k^- and ζ_k^+ are the lower and upper limitations of the i -th state, respectively. Furthermore, ζ_F and ζ_R denote the ranges of the restricted and forbidden state, respectively. In the restricted state, the updated values of joint angles decrease as shown in Eqs. (59) and (60), and the joint angle update value becomes zero in the forbidden state.

2) *Joint Torque*: The joint torque limitation cannot be ignored while calculating the trajectory. From the Eq. (5), the joint torque in the steady state can be expressed as follows:

$$\begin{aligned} \tau_{joint} = & -\mathbf{J}_{rotor}^T \begin{bmatrix} \mathbf{F}_{rotor} \\ \mathbf{M}_{rotor} \end{bmatrix} \\ & - \sum_{i=1}^{N_{contact}} \mathbf{J}_{contact_i}^T \begin{bmatrix} \mathbf{F}_{contact_i} \\ \mathbf{M}_{contact_i} \end{bmatrix} - \sum_{i=1}^{N_{part}} \mathbf{J}_{part_i}^T(\mathbf{q}) m_{part_i} \mathbf{g}. \end{aligned} \quad (61)$$

Note that $\ddot{\mathbf{q}}$, $\ddot{\xi}$, and \mathbf{l}_{joint} are assumed to be zero, as the maneuvering of the joint motion of the aerial manipulator is sufficiently slow. From the relationship in Eq. (61), the joint torque constraint is given by

$$\delta\tau^- \leq \mathbf{J}_{\tau_i} \delta\zeta_k \leq \delta\tau^+, \quad (62)$$

where the lower and upper limitations $\delta\tau^-$, $\delta\tau^+$ are also expressed using the velocity damper. Furthermore, \mathbf{J}_{τ_i} is the Jacobian for the joint torque.

3) *Thrust*: For the robot equipped with rotors, the thrust limitation is critical for the maneuvering of joint motion during a flight and perching. Therefore, the constraint is given by

$$\delta\lambda^- \leq \mathbf{J}_\lambda \delta\zeta_k \leq \delta\lambda^+, \quad (63)$$

where $\delta\lambda^-$ and $\delta\lambda^+$ are also expressed using the velocity damper. Then, the upper thrust limitation during perching $\bar{\lambda}^+$ is expressed as follows:

$$\bar{\lambda}^+ = \lambda_{max} - \bar{\mathbf{Q}}_{perch}^{-1}(\mathbf{q}) \begin{bmatrix} \frac{1}{\mu_{xy}} \sqrt{F_{ee_x}^2 + F_{ee_y}^2} \\ 0.0 \\ 0.0 \\ 0.0 \end{bmatrix}, \quad (64)$$

where λ_{max} is the thrust limitation that depends on a rotor module. μ_{xy} is the static friction coefficient. Note that $\bar{\lambda}^- = 0$ during perching.

4) *Stability*: The rotor arrangement is varied when the rotor-distributed robots maneuver with joint motion, and the robot cannot fly in the vicinity of a specific posture. To address this problem, we use the manipulability measure as follows:

$$\rho_{stable} = \sqrt{\det\{\bar{\mathbf{Q}}(\zeta)\bar{\mathbf{Q}}(\zeta)^T\}}, \quad (65)$$

where robots stabilize as ρ_{stable} increases. By differentiating the relationship, the constraints for the stability of a rotor-distributed robot is obtained as follows:

$$\delta\rho_{stable} = \mathbf{J}_{stable} \delta\zeta_k \geq -\gamma_{stable} \frac{\rho^- - \rho_F}{\rho_R - \rho_F}, \quad (66)$$

where the velocity damper is used for this constraint. γ_{stable} is the damping gain parameter for stability.

5) *Collision Avoidance*: Hardware interference can critically damage the robots. To avoid collisions, we approximate the robot model using simple configurations (e.g., box, cylinder). As the robot is highly complex and it is difficult to consider a detailed model, the closest point is considered. Then, the linear constraint to avoid the collision can be expressed as:

$$\delta d_{collision} = \mathbf{n}(\mathbf{J}_1 - \mathbf{J}_2) \delta\zeta_k \geq -\gamma_{collision} \frac{d - d_F}{d_R - d_F}, \quad (67)$$

where \mathbf{n} is the unit vector between objects, and $\gamma_{collision}$ is the damping gain parameter used to avoid collisions.

6) *Airflow Interference*: The airflow interference of rotors significantly affects the stability of the robot. However, the airflow interference is considerably complex. Here, we assume the upper-stream and downstream of the rotors are cylindrical. Then, the distance between the i -th and j -th rotors has to satisfy the following relationship:

$$d_{rotor,i,j} = \|\mathbf{p}_{rotor,i} - \mathbf{p}_{rotor,j}\| - D_{rotor} > 0, \quad (68)$$

where D_{rotor} is the diameter of rotors. $\mathbf{p}_{rotor,i}$ and $\mathbf{p}_{rotor,j}$ are the i -th and j -th rotor positions, respectively. From the above equation, the linear constraint on the airflow interference is expressed using the same relationship in Eq. (67).

7) *Optimization Problem*: Based on the above discussion, the optimization problem in Eq. (50) is written as

$$\min_{\delta\zeta_k} \delta\zeta_k^T \mathbf{S}_1 \delta\zeta_k + (\mathbf{J}_e \delta\zeta_k - \delta\xi_{ee})^T \mathbf{S}'_2 (\mathbf{J}_e \delta\zeta_k - \xi_{ee}) + (\mathbf{J}_{foot} \delta\zeta_k - \delta\xi_{foot})^T \mathbf{S}''_2 (\mathbf{J}_{foot} \delta\zeta_k - \delta\xi_{foot}) \quad (69)$$

$$\text{s.t.} \quad (70)$$

Eqs. (58), (62), (63), (66), and (67).

By solving this problem, we calculate the trajectories such as those of the end-effector and achieve desired motions during perching in the experiments described in Sec. VII.

VI. SYSTEM ARCHITECTURE

This section, we introduce the proposed system for the rotor-distributed manipulator. (A) First, we explain that the control system architecture consists of the proposed flight/perching control and motion planner. (B) Next, we show the detailed configurations of the proposed RDM hardware and its inner communication system.

A. Control System Architecture

The entire control system architecture is shown in Fig. 6. First, the motion planner calculates the current target states such as the pose and joint angles based on the final target states using the differential kinematics framework as shown in Sec.V. Based on the current target states calculated by the motion planner, the position controller determines the target attitude such as the roll and pitch angles ϕ_d , θ_d , and vectoring apparatus angles α_i , β_i . Next, the attitude/altitude controller calculates the rotor thrust λ_{flight} to achieve a stable flight. This flight controller, composed of position and attitude/altitude controllers, uses the estimated values $\tilde{\mathbf{p}}$, $\tilde{\dot{\mathbf{p}}}$, $\tilde{\boldsymbol{\eta}}$, and $\tilde{\boldsymbol{\omega}}$. During perching, the QP-based controller calculates the current additional thrust to perch on ceilings λ_{perch} , t , using the estimated contact wrench $\tilde{\mathbf{W}}_{foot}$ by the foot wrench sensor. Here, the target joint and vectoring apparatus angles calculated by the motion planner and position controller are sent to servo motors, and the thrust command is sent to the rotor unit. The proposed manipulator performs motions using the above system.

B. Robot Configuration

1) *Hardware*: The main manipulator frames are made of carbon fiber reinforced plastics (CFRP) with a thickness of 1 mm, and the total mass is 3.35 kg. Furthermore, the detailed mass of each part is shown in Table IV. Next, each link is connected by servo motors (Dynamixel, XH430-W350-R), whose stall torque is 3.4 N in the roll and pitch directions. The vectoring apparatuses are connected to the main links using roll (Dynamixel, XH430-W350-R) and pitch joints (Dynamixel, XL430-W250-T), respectively. Here, the stall torque of the vectoring apparatus in the pitch direction is 3.4N since the roll joint moment is heavier than that of the pitch (stall torque: 1.5N) due to the dual rotor thrust difference. Therefore, the distance between rotors on the vectoring apparatus is the smallest possible value. The rotor

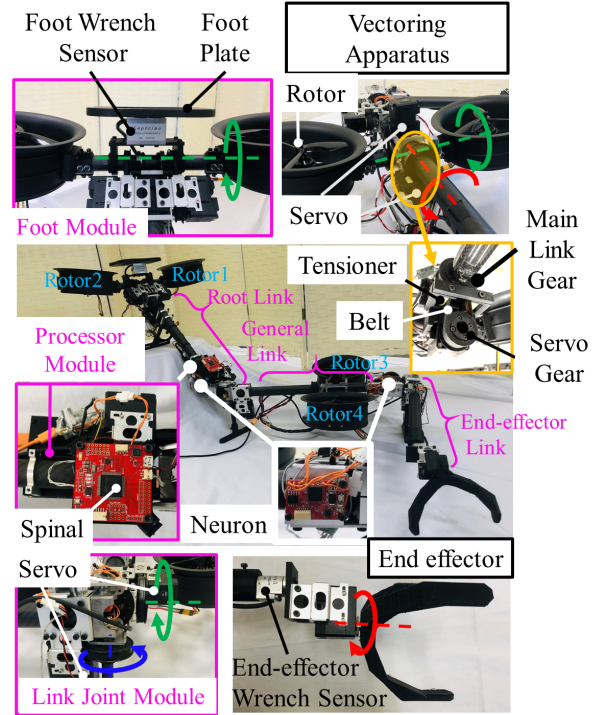


Fig. 7. Proposed platform of the RDM.

diameter on vectoring apparatus is 127 mm (T-Motor) and is actuated by a brushless motor (COBRA-2217), and can generate thrust from approximately 1-20 N. The footplate is approximated by a rectangle and equipped with a wrench sensor (CFS034CA301U, Leptrino) that can measure the force (rated capacity: ± 150 N in the x and y directions, and ± 300 N in the z direction) and moment (rated capacity: ± 4.0 Nm). Thus, the end-effector unit can be replaced by a drill, brush, or gripper. These units are also equipped with a wrench sensor (CFS018CA201, Leptrino) which can measure the force (rated capacity: ± 100 N in the x and y directions, and ± 200 N in the z direction) and moment (rated capacity: ± 1.0 Nm).

TABLE IV
CONFIGURATION OF AN AERIAL MANIPULATOR.

Component	Length[m]	Mass[kg]
Root Link	0.40	1.12
General Link	0.40	1.21
End effector Link	0.25	0.19
Link Joint Module	-	0.13
Processor Module	-	0.15
Total Link	-	3.35
Foot Module	-	0.35
Foot Plate Size	0.10 \times 0.15	

2) *Software*: We introduce the inner communication system for the proposed manipulator as shown in Fig. 8. On an external PC, the motion planner calculates the target states. The data is sent to the main processor using the wireless local area network. Here, the main processor on the robot, as shown in Fig. 7 is Latte Panda Alpha 864s (Intel m3-8100Y with quad cores, clock frequency:3.4GHz). Using

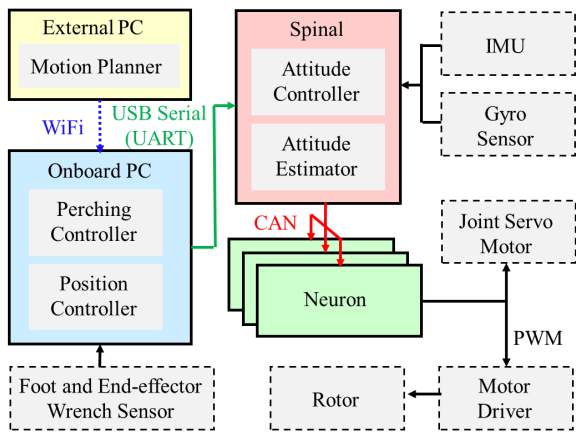


Fig. 8. Software system of the proposed RDM.

the data from an external PC and wrench estimated from the foot wrench sensor, the position and perching controller are running. The onboard PC communicates with the main control board (STM32F746, clock frequency:216MHz), called "Spinal" using serial communication (UART). On the main control board, the attitude controller and estimator are running, using the inertia moment unit (IMU) and gyro sensor, and determine the rotor thrust. Using the control area network (CAN), this main board communicates with the small control board on each link (STM32F413, clock frequency:100MHz) called "Neuron". Using RS485 and TTL signals, the servo motors on each link and vectoring apparatus are actuated by this neuron. Furthermore, the rotor unit is also actuated by the pulse width modulation (PWM) signal from the neuron.

In this section, we introduce the control system architecture and configurations of the proposed RDM. Using this system, we conduct the experiments in Sec. VII.

VII. EXPERIMENT

In this section, we evaluate the proposed RDM performance. (A) First, we evaluate the flight stability during flight. (B) Second, we confirm the perching stability (contact stability) such that the static friction and ZMP constraints are satisfied, during the maneuvering with joint motion. (C) Third, we added the external wrench at the end-effector during a flight and perching, and compared the end-effector feasibility during a flight with that during perching. (D) Finally, several manipulation tasks were conducted during perching on actual ceilings, such as drilling, painting walls, and opening a valve.

A. Flight Stability

We evaluated the stability during a flight. Here, the position control rate was 40 Hz on the onboard processor, and the attitude control rate was 200Hz on the spinal. During flight, the manipulator changed the configuration as shown in Fig. 9 (A). Here, the joints between links \mathbf{q} were varied from $[0.0, 0.0, 0.0, 0.0, 0.0, 0.0]^T$ to $[0.5, -0.5, 0.2, 0.8, 0.6, 0.0]^T$. We set the flight control parameters as shown in Table V. The position and attitude errors became less than ± 0.1 m and ± 0.05 rad. The vectoring apparatus was

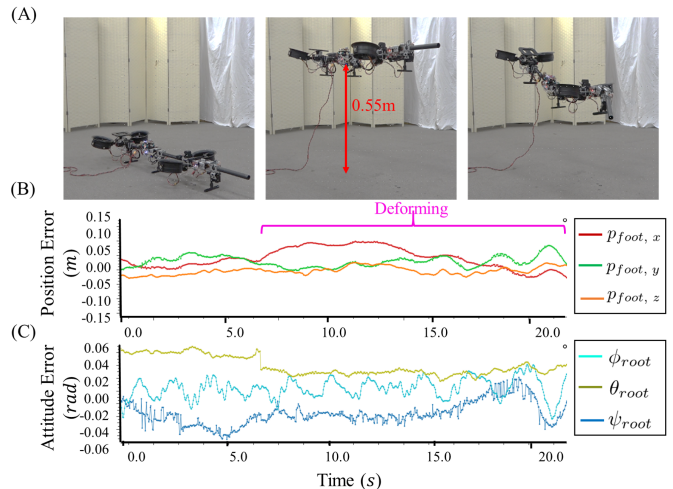


Fig. 9. (A) Rotor-distributed manipulator configuration change during flight. (B) Root position tracking errors. (C) Root attitude tracking errors.

TABLE V
FLIGHT CONTROL PARAMETERS.

Parameter	Value	Equation
\mathbf{W}_1	$\text{diag}[1, 1, 1]$	Eq. (27)
\mathbf{W}_2	$\text{diag}[20, 30, 90, 12.8, 600, 80, 100, 50, 20, 0.15, 1, 0.5]$	
$k_{P_x}, k_{I_x}, k_{D_x}$	4.6, 1.5, 7.0	Eq. (30)
$k_{P_y}, k_{I_y}, k_{D_y}$	7.0, 0.005, 10.5	
k_{ϕ_d}, k_{θ_d}	0.0, 1.0	Eq. (32)
k_{θ_1}, k_{ϕ_1}	0.0, 1.0	Eq. (36)
k_{θ_2}, k_{ϕ_2}	0.0, 0.0	

designed to rotate around the main link from -180 to 180 deg using a timing belt. This belt is equipped with a tensioner as shown in Fig. 7 to prevent it from being extended or slackened. The elasticity of the belt caused undesired angles of the vectoring apparatus, and the flight of aerial robots became unstable.

The root mean square errors (RMSEs) of the root position \mathbf{p}_{foot} , and attitude $\boldsymbol{\eta}_{foot}$ during the flight were (0.057 m, 0.033 m, 0.012 m, 0.017 rad, 0.036 rad, 0.039 rad) as shown in Table VI. In this experiment, the proposed controller could stabilize the RDM flight sufficiently.

TABLE VI
RMSE OF THE PROPOSED MANIPULATOR DURING FLIGHT.

	Position (m)	Attitude (rad)
x	0.057	0.017
y	0.033	0.036
z	0.012	0.039

B. Perching Stability

We evaluated the manipulator stability during the perching motion. The proposed perching controller calculates the additional thrust using an onboard processor at the rate of 40Hz. Here, we used the OSQP solver to optimize the QP problem in Eq. (49).

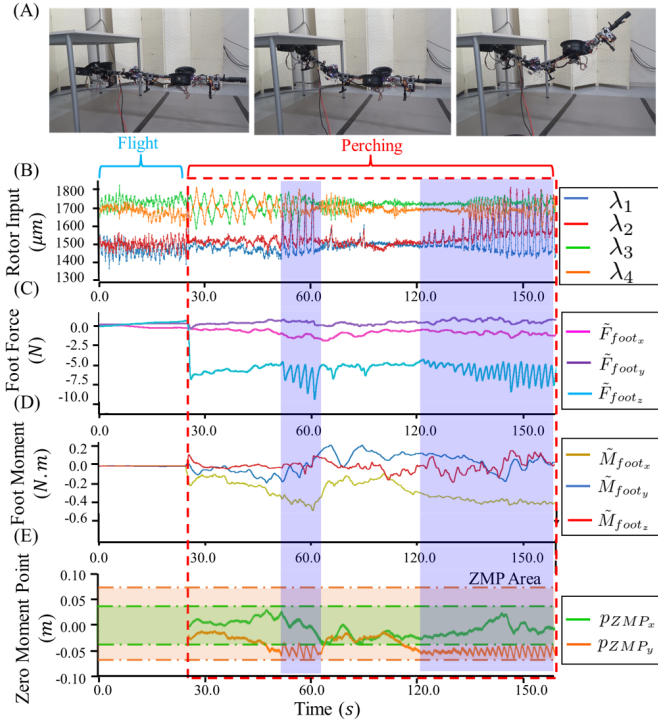


Fig. 10. (A) Transition from flight to perching and configuration change during perching. (B) Rotor inputs (C) Foot force observed by a wrench sensor. (D) Foot moment observed by a wrench sensor. (E) Foot ZMP.

We set the perching control parameters to prevent slipping and peeling from ceilings, as shown in Table VII. Here, the estimated force and torque by the wrench sensor shows significant amount of noise at times. The controller is required to generate an excessive thrust for perching. In this situation, the target rotor thrust exceeds the upper thrust limitation, and the manipulator can become unstable. Therefore, the infinite impulse response (IIR) filter, whose cutoff frequency is 1Hz, was used to smoothen the data.

We experimentally achieved a stable maneuvering with the joint motion of the proposed manipulator during perching, as shown in Fig. 10 (A). Here, the manipulator approached the ceiling and could smoothly shift from flight mode to perching mode at 27s. During the transition from a flight to perching, the rotor inputs were significantly increased to suppress the unstable contact such as slipping and peeling from the ceilings. The thrust of the foot rotors became approximately 1.4 times

TABLE VII
PERCHING CONTROL PARAMETERS.

Parameter	Value	Equation
N	$\text{diag}[1.0, 1.0, 1.0, 1.0]$	Eq.(37)
U_{mask}	$\text{diag}[1.0, 0.0, 0.0, 0.0]$	Eq. (38)
Q_{perch}	$Q(q)\text{diag}[1, 1, 0, 0]$	
ϵ_z	1.0	Eq. (39)
μ_x, μ_y	0.9	Eq. (40)
μ_z	0.5	Eq. (41)
H_x, H_y	0.04, 0.07	Eqs.(42)
$\delta\lambda_{perch}$	$[5.0, 5.0, 5.0, 5.0]^T$	Eq. (48)

larger than that during the flight for a moment, as shown in Fig. 10 (B). However, the manipulator became stable after that, and the foot rotor thrust decreased and becomes as large as that of the flight. This result shows that the thrust and consumption power for stable perching decreases owing to the ceiling effect. However, the rotor thrust fluctuated from 52s to 62s and from 135s to 160s when p_{ZMP_x} approached the boundaries during maneuvering with joint motion. This is because the controller had to increase the thrust to prevent the footplate from peeling from the ceilings. In this situation, power consumption also increased. During perching, the foot force \tilde{F}_{foot_x} , \tilde{F}_{foot_y} , \tilde{F}_{foot_z} and the moment \tilde{M}_{foot_z} satisfied the static friction constraints in Eqs. (39), (40), and (41) with a margin, as shown in Figs. 10 (C) and (D). Furthermore, the ZMP was within the footplate area, as shown in Fig. 10 (E). These results reveal that the footplate can perch on the ceiling with a significant amount of stability. Here, the rotor thrust during perching is equal to the thrust during flight, although the \tilde{F}_{foot_z} increased to fix the footplate on the ceiling.

C. End-Effector Evaluations

For the manipulation tasks, it is critical to evaluate the end-effector performance. Here, we conducted two experiments: (1) we added the external wrench at the end effector to evaluate the feasible wrench, and (2) compared the end-effector pose tracking stability during a flight with perching.

1) *External Wrench at the End-effector*: For manipulation tasks, it is critical to evaluate stability and feasible wrench when the external wrench is added to the end-effector. Therefore, we pushed and pulled the end-effector in the x , y , and z directions during the flight and perching without the external wrench observation control as shown in Figs.11 and 12.

In the flight experiment, the added wrench in the end-effector coordinate is shown in Figs.11 (B) and (C). Here, we focused on the time from 5.5 to 8.0s. The absolute values of the average end-effector force $F_{ee, x}$, $F_{ee, y}$, and $F_{ee, z}$ were 3.75, 1.76, and 3.42 N. As shown in Fig.11 (D), the foot position was varied under external wrench disturbances, and the standard deviation of the foot position in the x , y , and z directions were 0.0416, 0.0281, and 0.0220 m, respectively, as shown in Table.IX.

In the perching experiment, the added end-effector wrench is shown in Figs.12 (B) and (C). Here, the time from 22 to 24s was considered. The absolute values of the average forces during this time were 25.1, 8.4, and 16.8 N. In this configuration, the feasible force $F_{ee,y}$ was comparatively smaller than $F_{ee,x}$ and $F_{ee,z}$ owing to the yaw control feasibility. This is

TABLE VIII
FEASIBLE FORCE AT THE END-EFFECTOR.

	Flight		Perching	
	Average	Peak	Average	Peak
$ F_{ee, x} $	3.75	7.48	25.1	41.8
$ F_{ee, y} $	1.76	2.62	8.4	15.9
$ F_{ee, z} $	3.42	6.07	16.8	32.1
$ M_{ee, x} $	0.054	0.082	0.736	1.266
$ M_{ee, y} $	0.620	0.975	0.298	0.560
$ M_{ee, z} $	0.0203	0.197	0.943	1.520

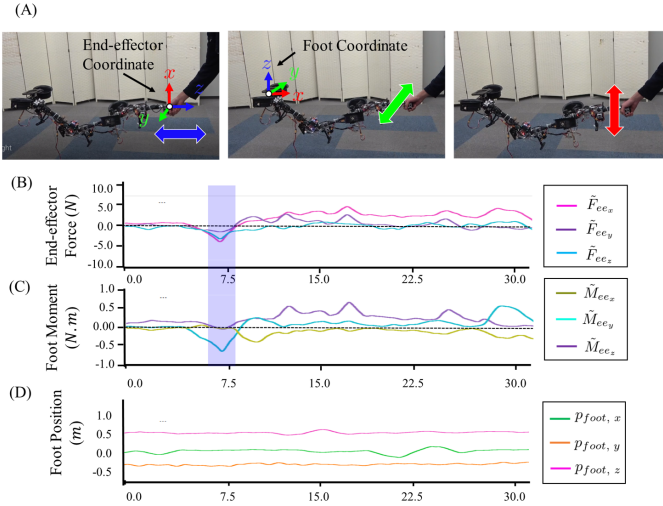


Fig. 11. Manipulator flight stability under end-effector wrench disturbances. (A) The end-effector is pushed and pulled; (B) end-effector force observed by a wrench sensor; (C) end-effector moment observed by a wrench sensor; and (D) foot position observed by a motion capture system (ground truth).

TABLE IX
STANDARD DEVIATION OF THE FOOT POSITION DURING FLIGHT AND PERCHING.

	Flight	Perching
x	0.0416	0.0009
y	0.0281	0.0011
z	0.0220	0.0004

because a small $F_{ee,y}$ generates a large moment in the yaw direction at the origin of the foot coordinate. Therefore, the static friction moment constraint could not be satisfied, and the footplate slips in the yaw direction. Owing to the external disturbance, the foot force $F_{foot,z}$ in the foot coordinate increases significantly as shown in Fig.12 (D) to prevent the foot from slipping and peeling from the ceilings. Owing to this thrust increase, the static friction and ZMP constraints were satisfied as shown in Figs.12 (D), (E), and (F). Furthermore, the standard deviation of the foot position during perching in the x -, y -, and z - directions were 0.0009, 0.0011, and 0.0004m, respectively. They were significantly smaller than that during flight as shown in Fig.12 (F) and Table VIII. This phenomenon was observed even when the added external force during perching was larger than that during the flight. These experiments clarified that the manipulator generates a larger wrench at the end-effector by being fixed on ceilings.

2) *Stability at the End-Effector*: We developed an RDM with a perching ability to improve the end-effector stability. To evaluate the end-effector stability during flight and perching, we compared the position and attitude tracking ability at the end-effector. Here, p_{ee} and η_{ee} were the position and attitude at the end effector, respectively. The target pose is determined by the planner. Note that we used feedback control not in the motion planner but in position and attitude control. As shown in Fig. 13 (A), the end-effector during flight became unstable, especially from 5 to 16 s owing to disturbances such as the ground effect,

and the maximum amplitudes of position and attitude errors were over 0.1 m and 0.3 rad, respectively. It is difficult for aerial robots, especially during maneuvering with joint motion, to stabilize the position under disturbances owing to the complexity of the rotor airflow dynamics. However, the end-effector during perching became significantly stable, and the end-effector did not vibrate. Owing to the fixed root approach, the end-effector position and attitude errors were generally less than 0.05 m and 0.1 rad as shown in Fig. 13 (B). Furthermore, the position and attitude RMSE during flight and perching were [0.055 m, 0.076 m, 0.069 m, 0.0019 rad, 0.0003 rad, 0.0004 rad] and [0.0032 m, 0.029 m, 0.019 m, 0.0002 rad, 0.0001 rad, 0.0005 rad] as shown in Table. X. These results clarified that the end-effector position tracking performance significantly improved due to the fixed-root approach.

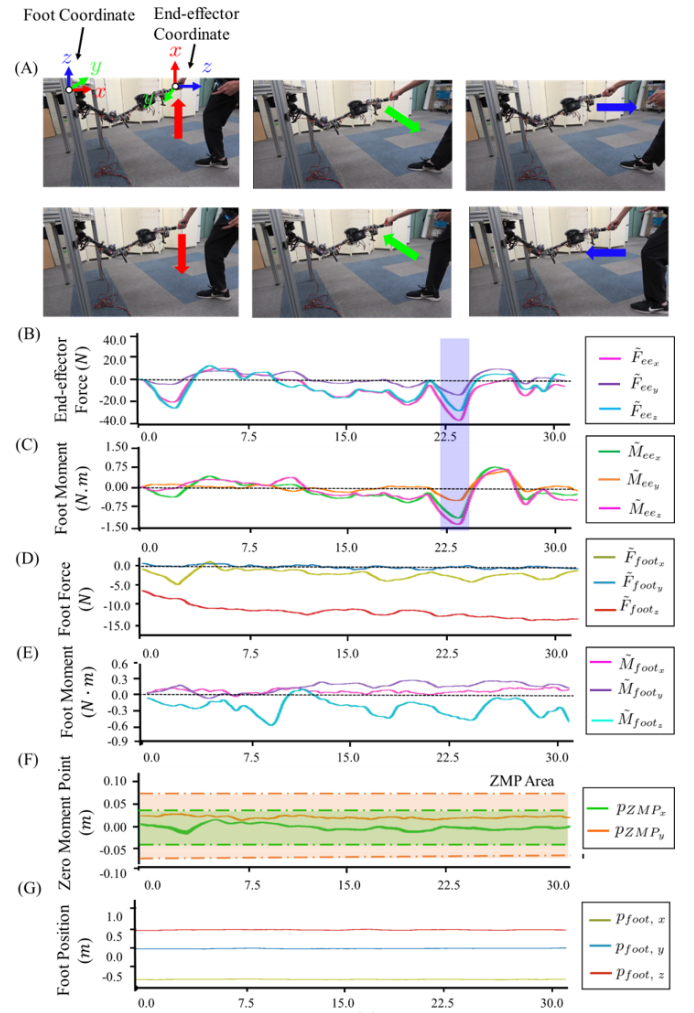


Fig. 12. Manipulator stability under end-effector wrench disturbances. (A) We push and pull the end-effector. (B) End-effector force observed by a wrench sensor. (C) End-effector moment observed by a wrench sensor. (D) Rotor inputs (E) Foot force observed by a wrench sensor. (F) Foot moment observed by a wrench sensor. (G) Foot ZMP. (H) Foot position observed by the motion capture system (ground truth)

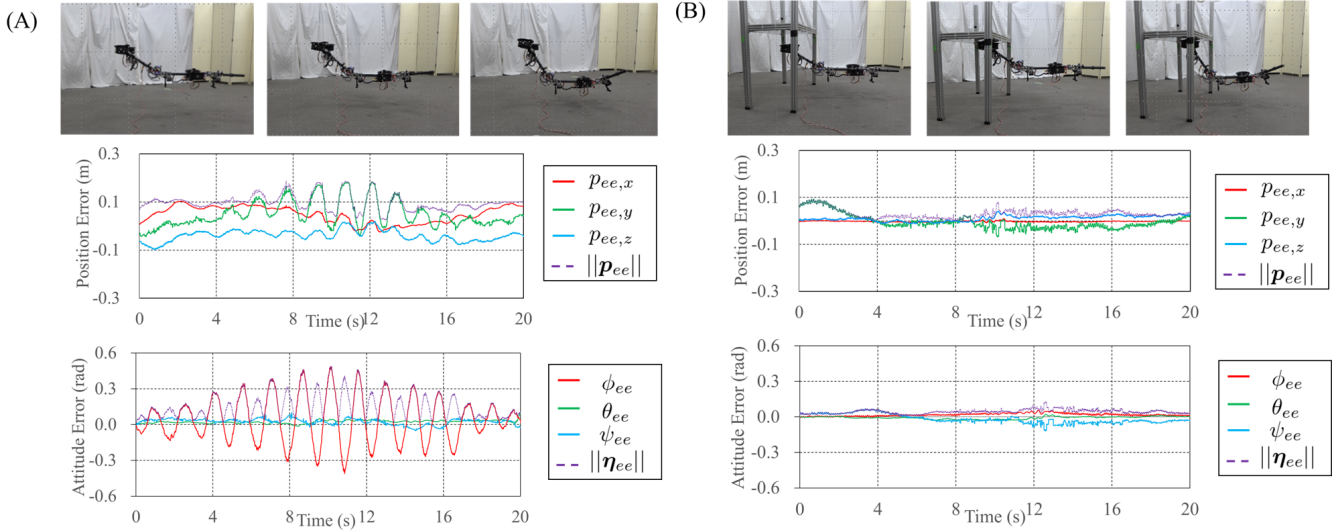


Fig. 13. Comparison of the end-effector position and attitude of the proposed rotor-distributed manipulator. (A) during flight (B) during perching. In these experiments, the baselink position and attitude are controlled by the real-time feedback method as shown in Sec. IV. However, the joint angles are determined by a feed-forward motion planner.

TABLE X
RMSE AT THE END-EFFECTOR DURING FLIGHT AND PERCHING.

	Flight	Perching
x	0.0552	0.00320
y	0.0759	0.0286
z	0.0688	0.0191
ϕ	0.0019	0.0002
θ	0.0003	0.0001
ψ	0.0004	0.0005

D. Perching Manipulation Tasks

Using the proposed control and planning method for the rotor-distributed manipulator, we achieved manipulation on the ceiling as shown in Fig. 14. In Fig. 14 (A), the manipulator conducted a drill manipulation. This manipulation task is classified as the point-contact task, and the end-effector can generate sufficient force to drill several holes in a wood board, and the position errors of these holes became approximately 0.01m. To increase the precision at the end-effector, real-time position feedback control would be one of the most useful approaches. In addition, the manipulator perches on the actual ceiling and paints walls using a brush, as shown in Fig.14 (B). This task is classified as the sliding task, and the sliding area length was over 0.5m in the vertical direction. Finally, this manipulator conducted a more complex manipulation task. This robot generated the moment at the end-effector gripper and opened a valve, as shown in Fig.14 (C). These experiments revealed the versatility of the proposed manipulator. In these experiments, the power of the robot was supplied by a cable.

VIII. CONCLUSION

In this study, we developed a minimal RDM configuration for perching. Based on the proposed system, we demonstrated that the RDM achieved stable maneuvering with joint motion during flight/perching and performed several manipulation

tasks. The following are the three key contributions of our approach: (1) Considering the aerial ZMP and end-effector reachability, we proposed a quadrotor-based RDM as the minimal configuration for an RDM and demonstrated that the realized end-effector feasible wrench and reachability of the RDM were significantly better than those of the conventional RCMs. (2) Using the proposed QP-based controller considering the foot contact conditions, the end-effector became more precise and generated a larger wrench during perching. Furthermore, this control method decreased the desired thrust and power consumption for perching using the ceiling effect. This controller can also be adopted for conventional aerial robots. (3) The proposed RDM achieved several manipulation tasks on actual ceilings using the proposed motion planning method considering constraints such as the perching force.

In a future work, we could further improve the precision at the end-effector and decrease the desired thrust and power consumption during perching. For more precise manipulation, we would develop a real-time feedback controller for the end-effector position based on the proposed motion planner. To decrease the thrust and power consumption, the thrust in the horizontal directions would be utilized to compensate for the external disturbances at the end-effector. In the proposed controller, only vertical force is used to perch on surfaces, as this approach is comparatively easy to stabilize the robot during perching. However, this controller requires a significant perching force when the external disturbance is added at the end-effector. This is because the feasible static friction to prevent slipping is comparatively small. To increase energy efficiency and generate a larger wrench at the end-effector, a control approach which uses both horizontal-direction thrust and static friction is required. Furthermore, we could extend the perchable environment, such as side walls or pipes, and achieve dual-arm manipulation for more complex manipulation tasks. We believe that our proposed system could extend

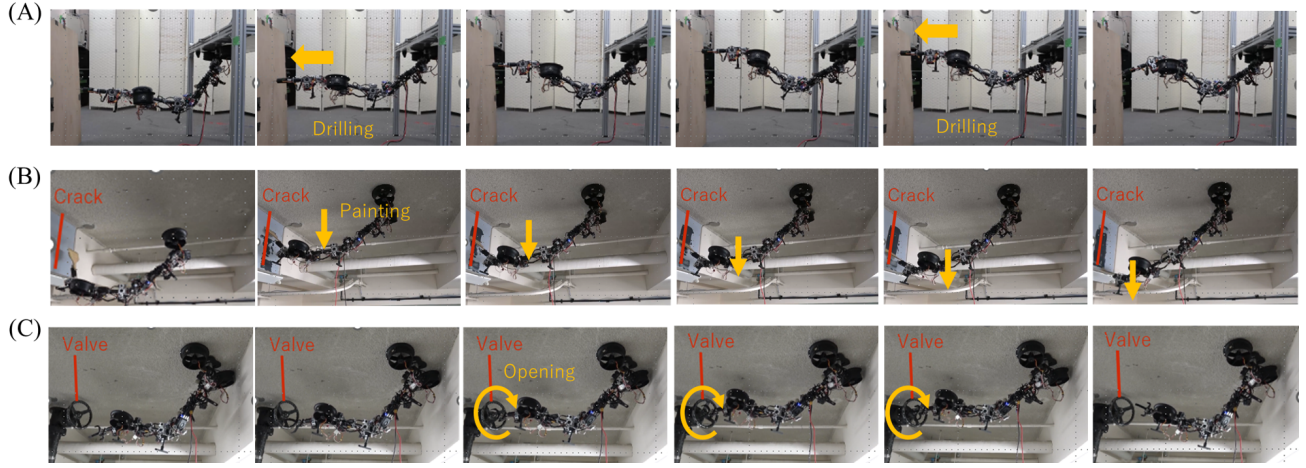


Fig. 14. Manipulation tasks by rotor-distributed aerial manipulator on the ceilings: (A) drill sampling, (B) painting walls and (C) opening a valve.

the applications of aerial manipulators, such as structural inspections and repairs.

APPENDIX A

FLIGHT STABILITY OF ROTOR DISTRIBUTED ROBOTS

The rotor force and moment at the \mathbf{p}_{AZMP} can be expressed as

$$\mathbf{F}_{rotor,AZMP} = \sum_{i=1}^{N_{rotor}} \mathbf{F}_{rotor,i}, \quad (71)$$

$$\mathbf{M}_{rotor,AZMP} = \sum_{i=1}^{N_{rotor}} (\mathbf{p}_{rotor,i} - \mathbf{p}_{AZMP}) \times \mathbf{F}_{rotor,i}, \quad (72)$$

where the stable control can be achieved where the moments caused by rotors in the roll and pitch directions are zeros. Then, $\mathbf{p}_{AZMP_{xy}}$ is given by

$$\mathbf{p}_{AZMP_{xy}} = \frac{\sum_{i=1}^{N_{rotor}} \mathbf{p}_{rotor,i_{xy}} F_{rotor,i_z}}{\sum_{i=1}^{N_{rotor}} F_{rotor,i_z}}. \quad (73)$$

Here, $F_{rotor,i_z} \geq 0$, and we define $\gamma_i = \frac{F_{rotor,i_z}}{\sum_{i=1}^{N_{rotor}} F_{rotor,i_z}}$.

Then, the γ_i can be as follows:

$$\gamma_i \geq 0, \quad (74)$$

$$\sum_{i=1}^{N_{rotor}} \gamma_i = 1. \quad (75)$$

Based on the above discussion, $\mathbf{p}_{AZMP_{xy}}$ constraints to achieve a stable flight can be written as follows:

$$\mathbf{p}_{AZMP_{xy}} \in \sum_{i=1}^{N_{rotor}} \gamma_i \mathbf{p}_{rotor,i_{xy}} \quad (76)$$

We call this area the aerial support polygon and use it to evaluate the flight stability in Sec. II.

REFERENCES

- [1] Anibal Ollero, Marco Tognon, Alejandro Suarez, Dongjun Lee, and Antonio Franchi. Past, present, and future of aerial robotic manipulators. *IEEE Transactions on Robotics*, 38(1):626–645, 2021.
- [2] K. Kondak, F. Huber, M. Schwarzbach, M. Laiacker, D. Sommer, M. Bejar, and A. Ollero. Aerial manipulation robot composed of an autonomous helicopter and a 7 degrees of freedom industrial manipulator. In *2014 IEEE International Conference on Robotics and Automation (ICRA)*, pages 2107–2112, 2014.
- [3] H. W. Wopereis, J. J. Hoekstra, T. H. Post, G. A. Folkertsma, S. Stramigioli, and M. Fumagalli. Application of substantial and sustained force to vertical surfaces using a quadrotor. In *2017 IEEE International Conference on Robotics and Automation (ICRA)*, pages 2704–2709, 2017.
- [4] Miguel Ángel Trujillo, José Ramiro Martínez-de Dios, Carlos Martín, Antidio Viguria, and Anibal Ollero. Novel aerial manipulator for accurate and robust industrial ndt contact inspection: A new tool for the oil and gas inspection industry. *Sensors*, 19(6):1305, 2019.
- [5] Karen Bodie, Maximilian Brunner, Michael Pantic, Stefan Walser, Patrick Pfändler, Ueli Angst, Roland Siegwart, and Juan Nieto. An omnidirectional aerial manipulation platform for contact-based inspection. *arXiv preprint arXiv:1905.03502*, 2019.
- [6] Salua Hamaza, Ioannis Georgilas, Manuel Fernandez, Pedro Sanchez, Thomas Richardson, Guillermo Heredia, and Anibal Ollero. Sensor installation and retrieval operations using an unmanned aerial manipulator. *IEEE Robotics and Automation Letters*, 4(3):2793–2800, 2019.
- [7] T. Bartelds, A. Capra, S. Hamaza, S. Stramigioli, and M. Fumagalli. Compliant aerial manipulators: Toward a new generation of aerial robotic workers. *IEEE Robotics and Automation Letters*, 1(1):477–483, 2016.
- [8] Burak Yüksel, Saber Mahboubi, Cristian Secchi, Heinrich H. Bühlhoff, and Antonio Franchi. Design, identification and experimental testing of a light-weight flexible-joint arm for aerial physical interaction. In *2015 IEEE International Conference on Robotics and Automation (ICRA)*, pages 870–876, 2015.
- [9] Markus Ryll, Giuseppe Muscio, Francesco Pierri, Elisabetta Cataldi, Gianluca Antonelli, Fabrizio Caccavale, Davide Bicego, and Antonio Franchi. 6d interaction control with aerial robots: The flying end-effector paradigm. *The International Journal of Robotics Research*, 38(9):1045–1062, 2019.
- [10] Karen Bodie, Maximilian Brunner, Michael Pantic, Stefan Walser, Patrick Pfändler, Ueli Angst, Roland Siegwart, and Juan Nieto. Active interaction force control for contact-based inspection with a fully actuated aerial vehicle. *IEEE Transactions on Robotics*, 37(3):709–722, 2021.
- [11] Ramy Rashad, Davide Bicego, Jelle Zult, Santiago Sanchez-Escalonilla, Ran Jiao, Antonio Franchi, and Stefano Stramigioli. Energy aware impedance control of a flying end-effector in the port-hamiltonian framework. *IEEE Transactions on Robotics*, 38(6):3936–3955, 2022.
- [12] Carmine Dario Bellicoso, Luca Rosario Buonocore, Vincenzo Lippello, and Bruno Siciliano. Design, modeling and control of a 5-dof light-

- weight robot arm for aerial manipulation. In *2015 23rd Mediterranean Conference on Control and Automation (MED)*, pages 853–858, 2015.
- [13] Alejandro Suarez, Fran Real, Víctor M. Vega, Guillermo Heredia, Angel Rodríguez-Castaño, and Anibal Ollero. Compliant bimanual aerial manipulation: Standard and long reach configurations. *IEEE Access*, 8:88844–88865, 2020.
- [14] Gabriele Nava, Quentin Sablé, Marco Tognon, Daniele Pucci, and Antonio Franchi. Direct force feedback control and online multi-task optimization for aerial manipulators. *IEEE Robotics and Automation Letters*, 5(2):331–338, 2020.
- [15] R Cano, C Pérez, F Pruano, A Ollero, and G Heredia. Mechanical design of a 6-dof aerial manipulator for assembling bar structures using uavs. In *2nd RED-UAS 2013 workshop on research, education and development of unmanned aerial systems*, volume 218, 2013.
- [16] G. Heredia, A.E. Jimenez-Cano, I. Sanchez, D. Llorente, V. Vega, J. Braga, J.A. Acosta, and A. Ollero. Control of a multirotor outdoor aerial manipulator. In *2014 IEEE/RSJ International Conference on Intelligent Robots and Systems*, pages 3417–3422, 2014.
- [17] Matko Orsag, Christopher Korpela, Stjepan Bogdan, and Paul Oh. Dexterous aerial robots—mobile manipulation using unmanned aerial systems. *IEEE Transactions on Robotics*, 33(6):1453–1466, 2017.
- [18] Hannibal Paul, Ryo Miyazaki, Robert Ladig, and Kazuhiro Shimonomura. Landing of a multirotor aerial vehicle on an uneven surface using multiple on-board manipulators. In *2019 IEEE/RSJ International Conference on Intelligent Robots and Systems (IROS)*, pages 1926–1933, 2019.
- [19] Russ Tedrake. *Underactuated robotics: Algorithms for walking, running, swimming, flying, and manipulation*, 2023.
- [20] Daniel Mellinger, Quentin Lindsey, Michael Shomin, and Vijay Kumar. Design, modeling, estimation and control for aerial grasping and manipulation. In *2011 IEEE/RSJ International Conference on Intelligent Robots and Systems*, pages 2668–2673, 2011.
- [21] S. Park et al. Odar: Aerial manipulation platform enabling omnidirectional wrench generation. *IEEE/ASME Transactions on Mechatronics*, 23(4):1907–1918, Aug 2018.
- [22] Burak Yüksel, Cristian Secchi, Heinrich H Bühlhoff, and Antonio Franchi. Aerial physical interaction via ida-phc. *The International Journal of Robotics Research*, 38(4):403–421, 2019.
- [23] Markus Ryll, Giuseppe Muscio, Francesco Pierri, Elisabetta Cataldi, Gianluca Antonelli, Fabrizio Caccavale, Davide Bicego, and Antonio Franchi. 6d interaction control with aerial robots: The flying end-effector paradigm. *The International Journal of Robotics Research*, 38(9):1045–1062, 2019.
- [24] Pisak Chermprayong, Ketao Zhang, Feng Xiao, and Mirko Kovac. An integrated delta manipulator for aerial repair: A new aerial robotic system. *IEEE Robotics & Automation Magazine*, 26(1):54–66, 2019.
- [25] H. W. Wopereis, T. D. van der Molen, T. H. Post, S. Stramigioli, and M. Fumagalli. Mechanism for perching on smooth surfaces using aerial impacts. In *2016 IEEE International Symposium on Safety, Security, and Rescue Robotics (SSRR)*, pages 154–159, 2016.
- [26] Sensen Liu, Wei Dong, Zhao Ma, and Xinjun Sheng. Adaptive aerial grasping and perching with dual elasticity combined suction cup. *IEEE Robotics and Automation Letters*, 5(3):4766–4773, 2020.
- [27] Hai-Nguyen Nguyen, Robert Siddall, Brett Stephens, Alberto Navarro-Rubio, and Mirko Kovac. A passively adaptive microspine grapple for robust, controllable perching. In *2019 2nd IEEE International Conference on Soft Robotics (RoboSoft)*, pages 80–87, 2019.
- [28] Hao Jiang, Shiquan Wang, and Mark R Cutkosky. Stochastic models of compliant spine arrays for rough surface grasping. *The International Journal of Robotics Research*, 37(7):669–687, 2018.
- [29] Ludovic Daler, Adam Klaptocz, Adrien Briod, Metin Sitti, and Dario Floreano. A perching mechanism for flying robots using a fibre-based adhesive. In *2013 IEEE International Conference on Robotics and Automation*, pages 4433–4438, 2013.
- [30] Justin Thomas, Morgan Pope, Giuseppe Loianno, Elliot W Hawkes, Matthew A Estrada, Hao Jiang, Mark R Cutkosky, and Vijay Kumar. Aggressive flight with quadrotors for perching on inclined surfaces. *Journal of Mechanisms and Robotics*, 8(5):051007, 2016.
- [31] Haijie Zhang, Elisha Lerner, Bo Cheng, and Jianguo Zhao. Compliant bistable grippers enable passive perching for micro aerial vehicles. *IEEE/ASME Transactions on Mechatronics*, 26(5):2316–2326, 2021.
- [32] Tzu-Jui Lin, Siyu Long, and Karl A. Stol. Automated perching of a multirotor uav atop round timber posts. In *2018 IEEE/ASME International Conference on Advanced Intelligent Mechatronics (AIM)*, pages 486–491, 2018.
- [33] William RT Roderick, Mark R Cutkosky, and David Lentink. Bird-inspired dynamic grasping and perching in arboreal environments. *Science Robotics*, 6(61):eabj7562, 2021.
- [34] Kazuaki Yanagimura, Kazunori Ohno, Yoshito Okada, Eijiro Takeuchi, and Satoshi Tadokoro. Hovering of mav by using magnetic adhesion and winch mechanisms. In *2014 IEEE International Conference on Robotics and Automation (ICRA)*, pages 6250–6257, 2014.
- [35] F. J. Garcia-Rubiales, P. Ramon-Soria, B.C. Arrue, and A. Ollero. Magnetic detaching system for modular uavs with perching capabilities in industrial environments. In *2019 Workshop on Research, Education and Development of Unmanned Aerial Systems (RED UAS)*, pages 172–176, 2019.
- [36] Antonio E. Jimenez-Cano, Pedro J. Sanchez-Cuevas, Pedro Grau, Anibal Ollero, and Guillermo Heredia. Contact-based bridge inspection multirotors: Design, modeling, and control considering the ceiling effect. *IEEE Robotics and Automation Letters*, 4(4):3561–3568, 2019.
- [37] Vernon J Rossow. Effect of ground and/or ceiling planes on thrust of rotors in hover. 1985.
- [38] Xinkuang Wang, Shanshan Du, and Yong Liu. Research on ceiling effect of quadrotor. In *2017 IEEE 7th Annual International Conference on CYBER Technology in Automation, Control, and Intelligent Systems (CYBER)*, pages 846–851. IEEE, 2017.
- [39] Yasutada Tanabe, Masahiko Sugiura, Takashi Aoyama, Hideaki Sugawara, Shigeru Sunada, Koichi Yonezawa, and Hiroshi Tokutake. Multiple rotors hovering near an upper or a side wall. *Journal of Robotics and Mechatronics*, 30(3):344–353, 2018.
- [40] Stephen A Conyers, Matthew J Rutherford, and Kimon P Valavanis. An empirical evaluation of ceiling effect for small-scale rotorcraft. In *2018 International Conference on Unmanned Aircraft Systems (ICUAS)*, pages 243–249. IEEE, 2018.
- [41] Yi Hsuan Hsiao and Pakpong Chirattananon. Ceiling effects for surface locomotion of small rotorcraft. In *2018 IEEE/RSJ International Conference on Intelligent Robots and Systems (IROS)*, pages 6214–6219. IEEE, 2018.
- [42] Takuzumi Nishio, Moju Zhao, Fan Shi, Tomoki Anzai, Kento Kawaharazuka, Kei Okada, and Masayuki Inaba. Stable control in climbing and descending flight under upper walls using ceiling effect model based on aerodynamics. In *2020 IEEE International Conference on Robotics and Automation (ICRA)*, pages 172–178. IEEE, 2020.
- [43] Raymond Ung, Frédéric Bourgault, Matthew Donovan, and Raffaello D’Andrea. The distributed flight array. In *2010 IEEE International Conference on Robotics and Automation*, pages 601–607, 2010.
- [44] Bruno Gabrich, David Saldana, Vijay Kumar, and Mark Yim. A flying gripper based on cuboid modular robots. In *2018 IEEE International Conference on Robotics and Automation (ICRA)*, pages 7024–7030. IEEE, 2018.
- [45] Moju Zhao, Koji Kawasaki, Tomoki Anzai, Xiangyu Chen, Shintaro Noda, Fan Shi, Kei Okada, and Masayuki Inaba. Transformable multirotor with two-dimensional multilinks: Modeling, control, and whole-body aerial manipulation. *The International Journal of Robotics Research*, 37(9):1085–1112, 2018.
- [46] Yuhang Li, Yuhao Zhou, Junbin Huang, Zijun Wang, Shunjie Zhu, Kairong Wu, Li Zheng, Jiajin Luo, Rui Cao, Yun Zhang, and Zhifeng Huang. Jet-hr2: A flying bipedal robot based on thrust vector control. *IEEE Robotics and Automation Letters*, 7(2):4590–4597, 2022.
- [47] Moju Zhao, Tomoki Anzai, Fan Shi, Xiangyu Chen, Kei Okada, and Masayuki Inaba. Design, modeling, and control of an aerial robot dragon: A dual-rotor-embedded multilink robot with the ability of multi-degree-of-freedom aerial transformation. *IEEE Robotics and Automation Letters*, 3(2):1176–1183, 2018.
- [48] Hyunsoo Yang, Sangyul Park, Jeongseob Lee, Joonmo Ahn, Dongwon Son, and Dongjun Lee. Lasdra: Large-size aerial skeleton system with distributed rotor actuation. In *2018 IEEE International Conference on Robotics and Automation (ICRA)*, pages 7017–7023. IEEE, 2018.
- [49] Miomir Vukobratović and J Stepanenko. On the stability of anthropomorphic systems. *Mathematical biosciences*, 15(1-2):1–37, 1972.
- [50] Zhifeng Huang, Biao Liu, Jiapeng Wei, Qingsheng Lin, Jun Ota, and Yun Zhang. Jet-hr1: Two-dimensional bipedal robot step over large obstacle based on a ducted-fan propulsion system. In *2017 IEEE-RAS 17th International Conference on Humanoid Robotics (Humanoids)*, pages 406–411, 2017.
- [51] Kyunam Kim, Patrick Spieler, Elena-Sorina Lupu, Alireza Ramezani, and Soon-Jo Chung. A bipedal walking robot that can fly, slackline, and skateboard. *Science Robotics*, 6(59):eabf8136, 2021.
- [52] Dario Brescianini and Raffaello D’Andrea. Design, modeling and control of an omni-directional aerial vehicle. In *2016 IEEE international*

conference on robotics and automation (ICRA), pages 3261–3266. IEEE, 2016.

- [53] Tsuneo Yoshikawa. Manipulability of robotic mechanisms. The international journal of Robotics Research, 4(2):3–9, 1985.
- [54] Morteza Azad, Jan Babič, and Michael Mistry. Effects of the weighting matrix on dynamic manipulability of robots. Autonomous Robots, 43(7):1867–1879, 2019.
- [55] Fumio Kanehiro, Mitsuharu Morisawa, Wael Suleiman, Kenji Kaneko, and Eiichi Yoshida. Reactive leg motion generation method under consideration of physical constraints. Journal of the Robotics Society of Japan, 28(10):1251–1261, 2010.



Takuzumi Nishio is an Assistant Professor in the Department of Mechano-Informatics, School of Information Science and Technology, University of Tokyo. He received PhD degree from the Department of Interdisciplinary-Informatics, University of Tokyo, in 2022. His research interests are mechanical design, modeling and control of aerial robots, and vision-based recognition and motion planning of manipulators in field robotics.



and recognitionaction integrated system.

Kei Okada received BE in Computer Science from Kyoto University in 1997. He received MS and PhD in Information Engineering from The University of Tokyo in 1999 and 2002, respectively. From 2002 to 2006, he joined the Professional Programme for Strategic Software Project in The University Tokyo. He was appointed as a lecturer in the Creative Informatics at the University of Tokyo in 2006 and an associate professor in the Department of Mechano-Informatics in 2009. His research interests include humanoids robots, real-time 3D computer vision,



Moju Zhao is currently an Assistant Professor at The University of Tokyo. He received Doctor Degree from the Department of Mechano-Informatics, The University of Tokyo, 2018. His research interests are mechanical design, modelling and control, motion planning, and vision based recognition in aerial robotics. His main achievement is the articulated aerial robots which have received several awards in conference and journal, including the Best Paper Award in IEEE ICRA 2018.



Masayuki Inaba is a professor in the Department of Mechano-Informatics, School of Information Science and Technology, University of Tokyo. He graduated from the Department of Mechanical Engineering, University of Tokyo, in 1981, and received MS and PhD degrees from the Graduate School of Information Engineering, University of Tokyo, in 1983 and 1986. He was appointed as a lecturer in the Department of Mechanical Engineering, University of Tokyo, in 1986, an associate professor, in 1989, and a professor in the Department of Mechano-Informatics, in 2000. His research interests include key technologies of robotic systems and software architectures to advance robotics research. His research projects have included hand-eye coordination in rope handling, visionbased robotic server systems, remote-brained robot approach, whole-body behaviors in humanoids, robot sensor suits with electrically conductive fabric, and developmental software systems for evolving a robot body with a spine. He has received several awards including outstanding Paper Awards in 1987, 1998, and 1999 from the Robotics Society of Japan, JIRA Awards in 1994, ROBOMECH Awards in 1994 and 1996 from the Division of Robotics and Mechatronics of the Japan Society of Mechanical Engineers, and Fellow of the Robotics Society of Japan in 2008. Currently, he is a Chair of the Department of IRT Systems Study, Information and Robot Technology Research Initiative, University of Tokyo.